0.40 objective) with a LEICA DFC 300-FX digital camera were used for cell counting. The degenerating cells in the dentate gyrus (DG), Cornus Ammonis 3 (CA3), retrosplenial cortex (RCtx), and piriform cortex (PCtx) were counted using the analyze particle mode of Object-Image2.15 (US National Institutes of Health and at the University of Amsterdam). The analytical process was as follows: microscopic color images (each 0.16 mm^2) were opened using the Object-Image2.15 software and through a red channel image, degenerating neurons were selected by density slice mode. The degenerating neurons were always indicated by dense silver precipitates, which appear as black grains in their somata and cells with numerous fine grains in their somata and were counted using the analyze particles mode with several optional settings (i.e. 'minimal particle size of 20 pixels,' 'label particles,' 'outline particles,' 'ignore particles touching edge,' and 'include interior holes'). The numerical density of the degenerating cells was converted to a percentage of the cell number in non-Tg(NS) mice.

Immunohistochemical analysis

Serial sections (40 μm thick) were processed for immunostaining using a primary antibody against Pax6 (Inoue et al., 2000) (anti-Pax6 rabbit antibody 63, 1:500) [non-Tg(NS) ($n=5$), non-Tg(ST) ($n=5$), L/V-Tg(NS) ($n=5$), L/V-Tg(ST) ($n=5$)], Ki-67 (anti-Ki-67 rabbit serum, 1:50;YLEM, Roma, Italy, #PRO229) [non-Tg(NS) ($n=7$), non-Tg(ST) ($n=6$), L/V-Tg(NS) ($n=7$), L/V-Tg(ST) ($n=6$)], or double-cortin (DCX) (anti-DCX guinea pig antibody, 1:3000; Chemicon, CA, USA, #AB5910) [non-Tg(NS) ($n=9$), non-Tg(ST) ($n=8$), L/V-Tg(NS) ($n=9$), L/V-Tg(ST) ($n=8$)]. Free-floating sections were treated first with PBS containing 10% methanol and 3% H_2O_2 for 30 min at room temperature and rinsed in PBS. The sections were next treated with 3% normal goat serum in PBS containing 0.1% Triton X-100 for 2 h at room temperature and incubated for 48 h in the primary antibody solution at 4 °C. Then they were incubated with biotinylated goat anti-rabbit IgG (1:5000; Vector, CA, USA, #BA-1000) for Pax6 and Ki-67 or biotinylated goat anti-guinea pig IgG (1:500; Vector #BA-7000) for DCX for 2 h at room temperature. The immunoreactions with the ABC reagent (Vector) and the ImmunoPure Methal Enhanced DAB Substrate Kit (PIERCE, Rockford, IL, USA) were done according to the manufacturer's protocol. The sections were placed onto an MAS-coated slide glass (Matsunami, Osaka, Japan, #S9443), air-dried, dehydrated with ethanol and xylene, and coverslipped with HSR solution (International Reagents Corp., Kobe, Japan).

BrdU labeling

For the labeling of mitotic cells, the mice received an intraperitoneal injection of 5-bromo-2′-deoxyuridine (BrdU, Sigma, 15 mg/ml dissolved in 0.9% NaCl, 20 μl/g body weight) at 4:30–5:00 pm and were perfused 20 h after injection [non-Tg(NS) ($n=5$), non-Tg(ST) ($n=4$), L/V-Tg(NS) ($n=5$), L/V-Tg(ST) ($n=5$)]. This high dose of BrdU (300 mg/kg) is a specific, quantitative, and nontoxic marker of dividing cells in the adult DG (Cameron and McKay, 2001). Free-floating sections (40 μm thick) were made and incubated in 2 N HCl for 30 min at 37 °C. After being rinsed in borate buffer and PBS, sections were incubated with an anti-BrdU rat monoclonal antibody (1:500, abcam, Cambridge, MA, USA, #ab6326) overnight at 4 °C and then with the secondary antibody for 2 h at room temperature. The immunoreactions with the ABC reagent and DAB were performed as described above.

Quantification and stereology

Serial sections [six sections from each animal, Bregma −1.34 to −3.08 (Paxinos and Franklin, 2001)] (Supplementary Fig. 2) of one hemisphere were taken for stereological quantification of the dentate GCL, including the Pax6-, Ki-67-, DCX-, and BrdU-positive cells in the GCL and subgranular zone (SGZ, a two-cell-thick layer in the granule cell layer, is located close to the hilus or in the lower part of the GCL). For Pax6 or Ki-67 immunostaining, toluidine blue-stained serial sections were used to determine the total volume of the GCL. DAB-stained individual sections were viewed on a video monitor connected to a Zeiss Axiophot 2 microscope (2.5× NA 0.12 objective) with a 3CCD Fuji (Fujifilm, Tokyo, Japan) digital camera. Part of the GCL was delineated by drawing a line, using the programmed tool in Adobe Photoshop7.0 (Adobe Systems Inc., San Jose, CA, USA). The total area of the GCL was measured using Object-Image2.15, and the resultant volume (pixels) was converted into micrometers. Individual cells were visualized using the same system described above (10× NA 0.45 objective), and the marker-positive cells were counted in the GCL, SGZ, and hilus. The cells were counted by an observer blinded to the genotype and the treatment status.

Statistical analyses

For every parameter, the values were first calculated separately for each animal before the means and the standard error of the mean (SEM) were determined for the groups. The number of marker-positive cells in a fixed area (cells/mm^2) was converted to the percentage of the number of marker-positive cells in the non-Tg(NS) littermates. Data are expressed as the mean values ± SEM. All statistical analyses were performed with PRISM version 5.0a (GraphPad Software, La Jolla, CA, USA). The data were analyzed by a two-way analysis of variance (ANOVA) between genotypes (non-Tg, L/V-Tg) and treatments (non-stressed, stressed) and with a Bonferroni post hoc test. When an interaction was found, multiple comparisons were performed with the Tukey–Kramer test. Values of $P<0.05$ were considered significant.

Results

Establishment of a chronic intermittent restraint stress model

We first sought to establish an effective restraint tube-based chronic stress model (Supplementary Fig. 1) that causes long-lasting structural changes in the hippocampus. By the protocol with several weeks' continuous restraint stress, it has been pointed out that mice tend to be habituated to the stressor, making it difficult to precisely examine the effects of chronic stress (Kim and Han, 2006). A previous report also indicated that chronic intermittent restraint stress (CIRS) for 2 weeks affected adult neurogenesis in the hippocampus (Rosenbrock et al., 2005). We therefore determined that CIRS is an effective protocol to verify changes in neurogenesis and introduced a resting period during the chronic restraint protocol in which we assess the effectiveness of the stressor using the reduction in body weight gain and the hypertrophy of the adrenal glands as indices.

As a result, our CIRS protocol (Fig. 1) primarily reduced the body growth rate of both non-Tg and L/V-Tg mice under chronic stress (Fig. 2A, B). When the body weight gain, which is expressed as the difference between the end and the beginning of the experiment, was subjected to a two-way ANOVA, we found out a significant effect of treatment ($F_{1,46}=393.98$, $P<0.0001$), but not a genotype effect ($F_{1,46}=1.70$, $P=0.1990$) and no interaction ($F_{1,46}=2.14$, $P=0.1507$) in the short-term experiments. The analysis also revealed a significant effect of treatment ($F_{1,8}=25.66$, $P=0.0010$), but not a genotype effect ($F_{1,8}=0.08$, $P=0.7857$) and no interaction ($F_{1,8}=0.10$, $P=0.7618$) in the long-term experiments. Additionally, the unpaired t-test [non-Tg(ST) vs. L/V-Tg(ST)] revealed that the body weight gain of the L/V-Tg mice (−11.3 ± 0.6%) was significantly reduced compared with that of the non-Tg(ST) animals (−8.6 ± 1.0%) after short-term CIRS (two-tailed, $P=0.0266$; Supplementary Table 1). Although the body growth rate at the resting period was increased in

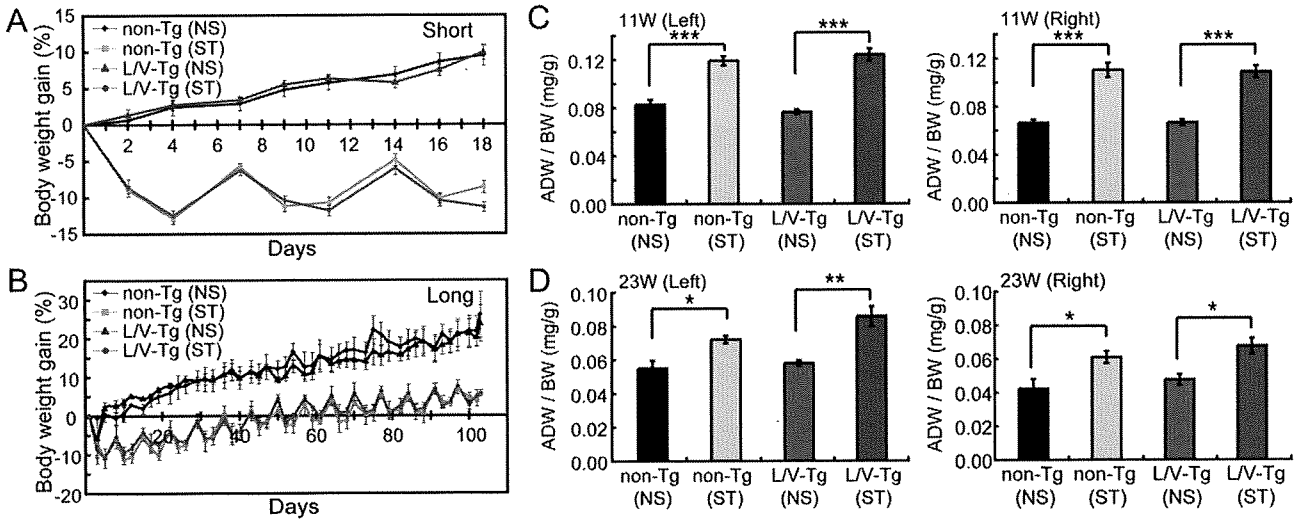

Fig. 2. Chronic intermittent restraint stress (CIRS) induces typical stress symptoms. (A, B) Changes in the body weight gain of mice in the stressed (ST) or non-stressed (NS) groups are plotted; (A) short term; (B) long term. The body weight gain 1 day before perfusion [expressed as the difference between the end and the beginning of the experiment, mean ± standard error of the mean (SEM)] is significantly reduced in stressed animals. (C, D) The left and right adrenal weights after short-term (C) or long-term (D) CIRS are significantly increased in the stressed groups. Data are expressed as the adrenal weight (mg) divided by the body weight (g) (ADW/BW, mean ± SEM). $^{*}P<0.05$, $^{**}P<0.01$, $^{***}P<0.001$ (Bonferroni, NS vs. ST). Non-Tg, transgenic negative mouse; L/V-Tg, transgenic mouse model of AD with overexpression of an FAD-type PS1; 11W, 11-week-old mice; 23W, 23-week-old mice.

every mouse, the rate of body weight change in the stressed groups showed a distinct fluctuating pattern for 15 weeks compared with that in the non-stressed groups (Fig. 2B). The weight of the right or left adrenal gland was also subjected to a two-way ANOVA, which revealed a significant effect of treatment [11-week-old mice (11W) left, $F_{1,45}=108.26$, $P<0.0001$; 11W right, $F_{1,45}=87.22$, $P<0.0001$; 23-week-old mice (23W) left, $F_{1,8}=28.17$, $P=0.0007$; 23W right, $F_{1,8}=20.57$, $P=0.0019$], but not of genotype effect (11W left, $F_{1,45}=0.24$, $P=0.6301$; 11W right, $F_{1,45}=0.02$, $P=0.8826$; 23W left, $F_{1,8}=4.17$, $P=0.0755$; 23W right, $F_{1,8}=0.57$, $P=0.4714$) and no interaction (11W left, $F_{1,45}=1.72$, $P=0.1963$; 11W right, $F_{1,45}=0.05$, $P=0.8275$; 23W left, $F_{1,8}=1.50$, $P=0.2555$; 23W right, $F_{1,8}=0.00$, $P=1.0000$) (Fig. 2C, D). Finally, the blood corticosterone levels in the groups with short-term chronic stress tended to increase (Supplementary Fig. 3). These results demonstrate that our short-term (3 weeks) and long-term (15 weeks) CIRS protocols can efficiently induce typical physical stress symptoms in mice.

CIRS increases the number of degenerating neurons

Because degenerating neurons appear in L/V-Tg mice without stress after 6 months of age (Chui et al., 1999), the obliteration of neuronal function in the neural circuit involved in cognitive function could be accelerated by the interaction of mutated genes and chronic stress. We thus examined whether stress accelerates neurodegeneration in the L/V-Tg mouse brain by means of the sliver staining: Degenerating neurons were indicated by dense silver precipitates appearing as black grains in their somata (shown by red arrowheads in Fig. 3B) and as cells with numerous fine grains in their somata (shown by red arrowheads in Fig. 3C). On the other hand, typical background signals were indicated by diluted brown particles (shown by a white arrowhead in Fig. 3B). As a result, in L/V-Tg mice degenerating neurons were selectively observed in the circuital areas that correlate with cognitive function. The number of degenerating neurons [% of non-Tg(NS)] was subjected to a two-way ANOVA, which revealed a significant effect of treatment ($F_{1,36}=9.58$, $P=0.0038$), genotype ($F_{1,36}=22.31$, $P<0.0001$), and an interaction ($F_{1,36}=7.18$, $P=0.0110$) in the DG; a significant effect of treatment ($F_{1,28}=8.88$, $P=0.0059$) and genotype ($F_{1,28}=10.13$, $P=0.0036$), but no interaction ($F_{1,28}=1.42$, $P=0.2435$) in the CA3; a significant effect of treatment ($F_{1,32}=25.68$, $P<0.0001$), but not of genotype ($F_{1,32}=2.09$, $P=0.1578$) and interaction ($F_{1,32}=2.19$, $P=0.1487$) in the RCtx; and a significant effect of genotype ($F_{1,27}=8.22$, $P=0.0079$), but not of treatment ($F_{1,27}=1.89$, $P=0.1810$) and interaction ($F_{1,27}=1.07$, $P=0.3108$) in the PCtx (Fig. 3D–G). After short-term CIRS (at 11 weeks of age), the number of degenerating neurons was significantly increased in the DG of L/V-Tg mice [Tukey–Kramer test, $P<0.0001$ vs. non-Tg(NS) and non-Tg(ST); $P<0.001$ vs. L/V-Tg(NS)] (Fig. 3D). The Bonferroni post hoc tests (NS vs. ST) revealed that CIRS increased the number of degenerating neurons in L/V-Tg mice [$P<0.05$, in the CA3 (Fig. 3E); $P<0.001$, in the RCtx (Fig. 3F)]. Especially in the hippocampus of the L/V-Tg(ST) mice, degenerating neurons were drastically increased in the SGZ of the DG, where considerable adult neurogenesis takes place (Fig. 3A). In non-Tg mice, the number of degenerating neurons was slightly increased after short-term CIRS only in the RCtx (Bonferroni test, $P<0.05$, NS vs. ST) (Fig. 3F).

After long-term CIRS (at 23 weeks of age), evidence of neurodegeneration was significantly accumulated in L/V-Tg mice compared with non-Tg mice in various brain regions, including the RCtx and the PCtx (Fig. 4D, E). The number of degenerating neurons was subjected to a two-way ANOVA. This analysis revealed a significant effect of treatment ($F_{1,52}=10.62$, $P=0.0020$), genotype ($F_{1,52}=15.45$, $P=0.0003$), but no interaction ($F_{1,52}=3.38$, $P=0.0719$) in the DG; a significant effect of treatment ($F_{1,44}=7.09$, $P=0.0108$), genotype ($F_{1,44}=19.50$, $P<0.0001$), and an interaction ($F_{1,44}=6.13$, $P=0.0172$) in the CA3; a significant effect of treatment ($F_{1,52}=6.07$,

Fig. 3. The number of degenerating neurons is increased in the brains of stressed animals (short-term). (A) Silver-stained sections of mice exposed to short-term chronic intermittent restraint stress (CIRS) (ST) or left untreated (NS). Scale bar, 100 μm. (B, C) High power pictures of degenerating neurons in the dentate gyrus (DG) (B) and piriform cortex (PCtx) (C) of L/V-Tg(ST) mice (corresponding to the insets in panel A, scale bar, 10 μm). Degenerating neurons are indicated by red arrowheads (B, C); typical background signal is indicated by a white arrowhead (B). (D–G) Graphs indicate the number of degenerating neurons [expressed as % of non-Tg(NS), mean ± SEM] in the DG (D), Cornus Ammonis 3 (CA3) (E), retrosplenial cortex (RCtx) (F), and PCtx (G). Statistical significance; DG [Tukey–Kramer test, $^{***}P<0.0001$ vs. non-Tg(NS); $\#\#\#P<0.0001$ vs. non-Tg(ST); $@@P<0.001$ vs. L/V-Tg (NS)] (D); CA3 (Bonferroni, NS vs. ST, $@P<0.05$) (E); RCtx (Bonferroni, NS vs. ST, $\#P<0.05$; $@@P<0.001$) (F). Note that most degenerating neurons in the DG of L/V-Tg(ST) mice are located in the SGZ. Non-Tg, transgenic negative mouse; L/V-Tg, transgenic mouse model of AD with overexpression of an FAD-type PS1; 11W, 11-week-old mice.

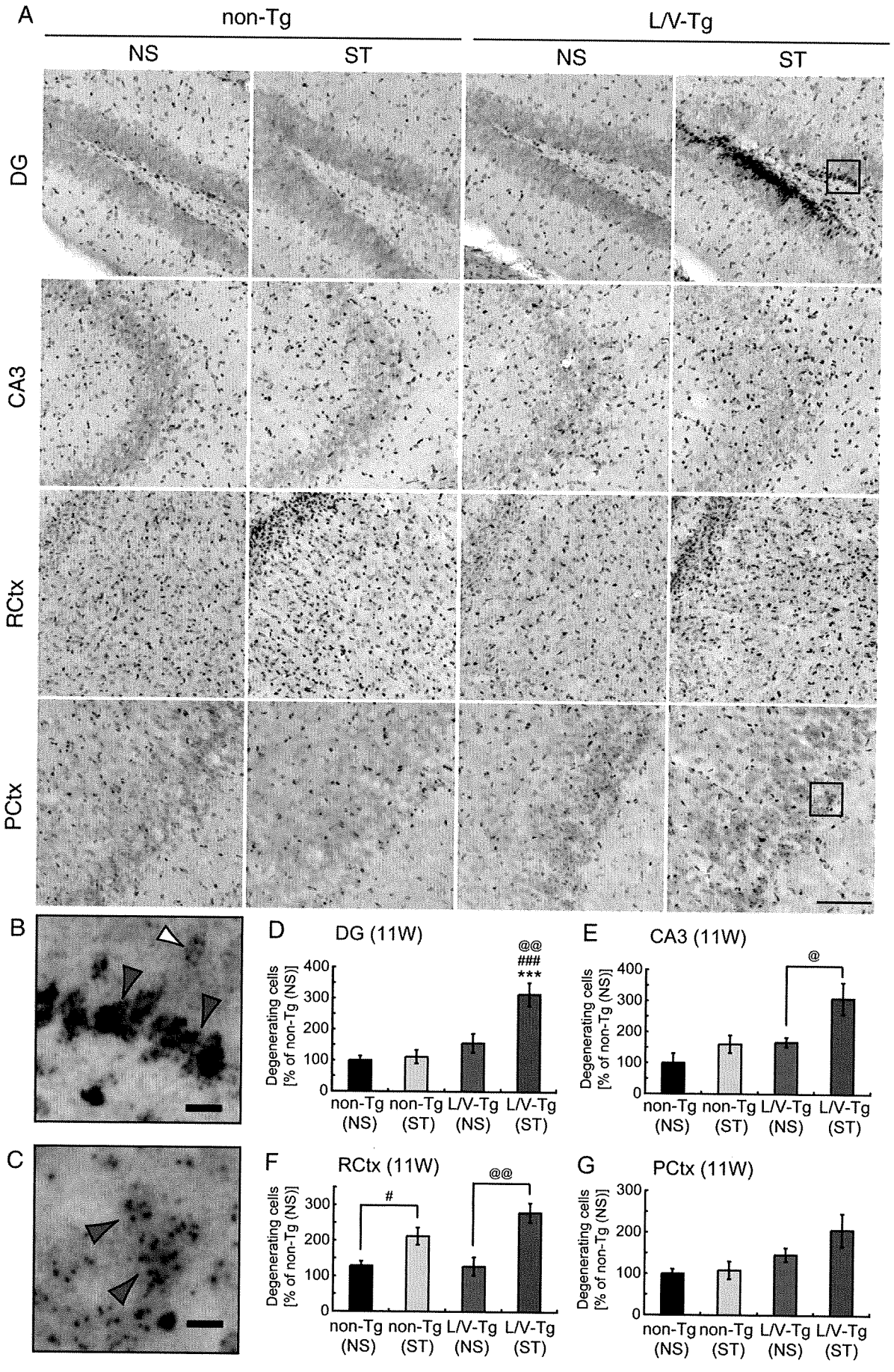
A
non-Tg
L/V-Tg
NS
ST
NS
ST
DG
CA3
RCtx
PCtx
B
C
D
DG (11W)
E
CA3 (11W)
F
RCtx (11W)
G
PCtx (11W)
Degenerating cells [% of non-Tg (NS)]
non-Tg (NS)
non-Tg (ST)
L/V-Tg (NS)
L/V-Tg (ST)
@@
###
***
@
#
@@

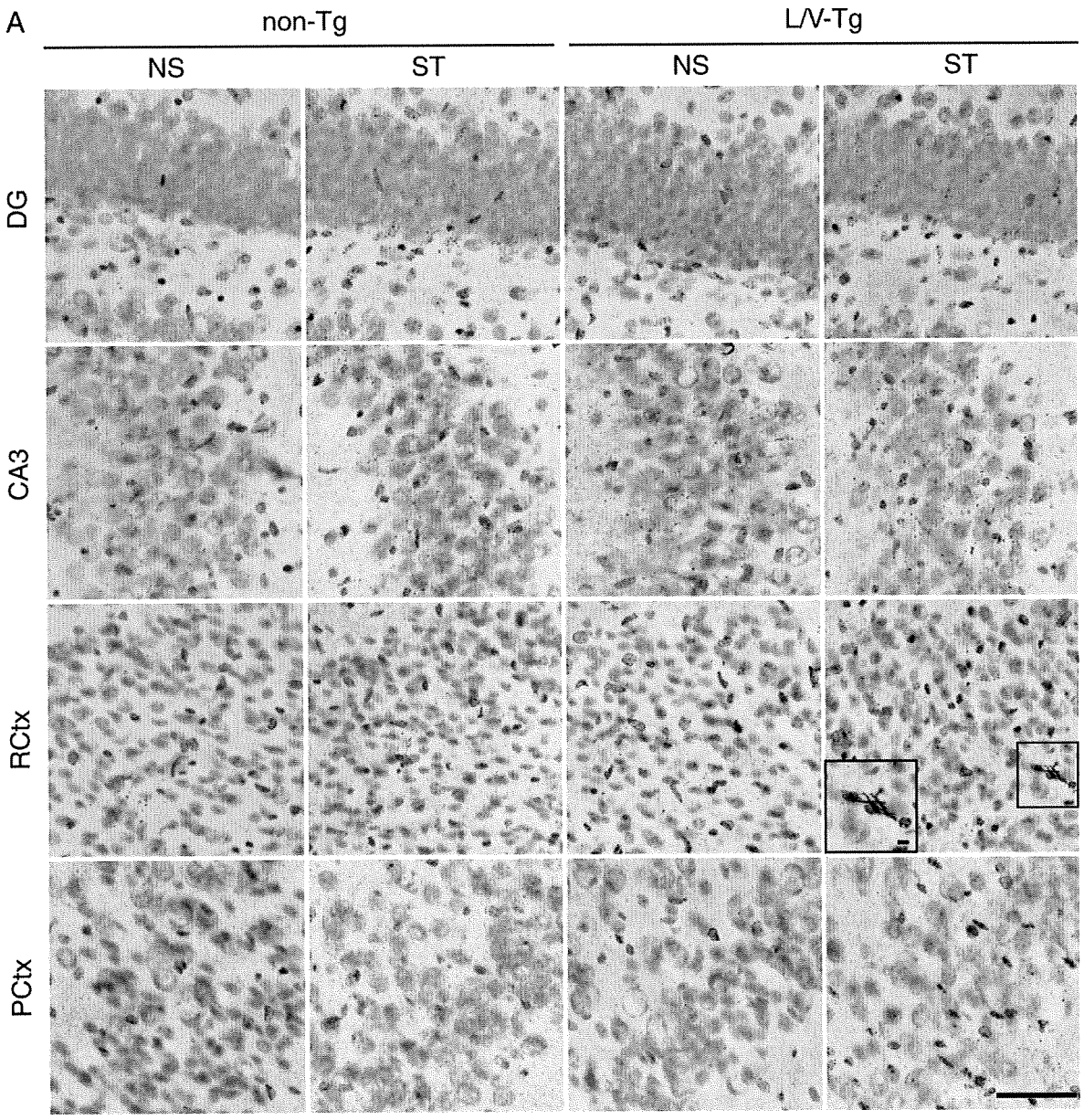
A
non-Tg
L/V-Tg
NS
ST
NS
ST
DG
CA3
RCtx
PCtx

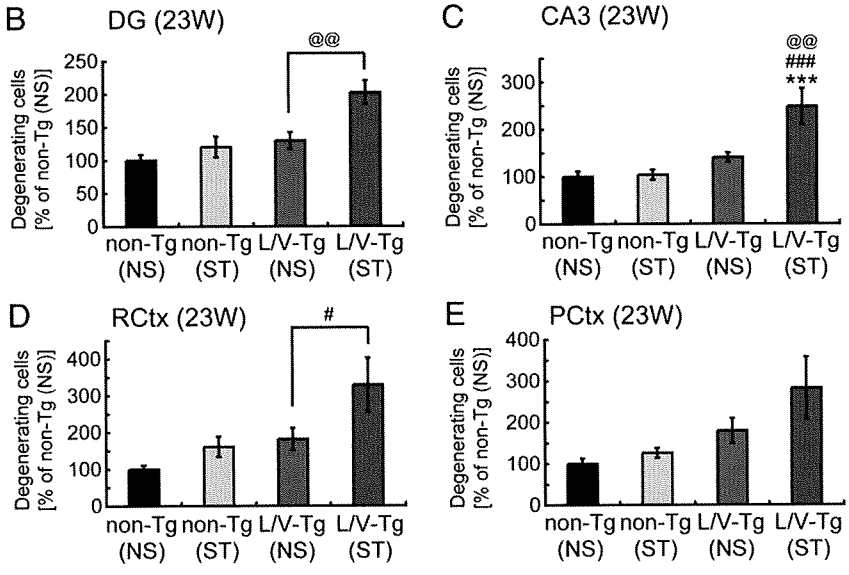
B
DG (23W)
@@
Degenerating cells [% of non-Tg (NS)]
250
200
150
100
50
0
non-Tg (NS)
non-Tg (ST)
L/V-Tg (NS)
L/V-Tg (ST)
C
CA3 (23W)
@@
###
***
Degenerating cells [% of non-Tg (NS)]
300
200
100
0
non-Tg (NS)
non-Tg (ST)
L/V-Tg (NS)
L/V-Tg (ST)
D
RCtx (23W)
#
Degenerating cells [% of non-Tg (NS)]
400
300
200
100
0
non-Tg (NS)
non-Tg (ST)
L/V-Tg (NS)
L/V-Tg (ST)
E
PCtx (23W)
Degenerating cells [% of non-Tg (NS)]
400
300
200
100
0
non-Tg (NS)
non-Tg (ST)
L/V-Tg (NS)
L/V-Tg (ST)

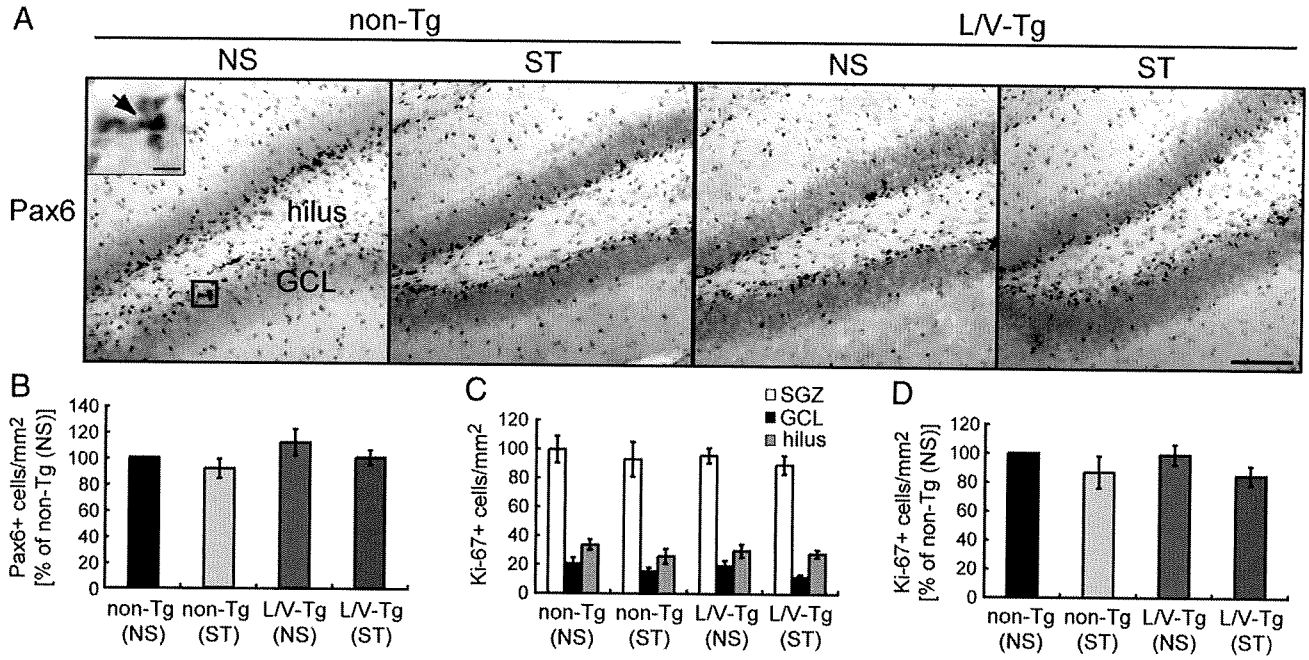

Fig. 5. Short-term chronic intermittent restraint stress (CIRS) slightly affects the number of granule neuron precursors and proliferating cells in the dentate gyrus. (A) Representative immunostaining of Pax6. Scale bar, 50 μm. Inset shows boxed region with a higher magnification (scale bar, 10 μm). An arrow indicates a Pax6+ cell. (B) The number of Pax6+ cells in the subgranular zone (SGZ) [mean ± SEM, % of non-Tg(NS)] tended to decrease in stressed (ST) animals. (C) The number of Ki-67+ cells in each hippocampal region [SGZ, hilus, and granule cell layer (GCL)]. Most Ki-67+ cells are observed in the SGZ, with considerable numbers localized to the hilar region and a few in the GCL. (D) The number of Ki-67+ cells in the GCL and SGZ is slightly decreased to a similar extent in non-Tg and L/V-Tg mice [mean ± SEM, % of non-Tg(NS)]. Non-Tg, transgenic negative mouse; L/V-Tg, transgenic mouse model of AD with overexpression of an FAD-type PS1.

$P=0.0171$) and genotype ($F_{1,52}=8.81$, $P=0.0045$), but no interaction ($F_{1,52}=1.04$, $P=0.3117$) in the RCtx; and a significant effect of genotype ($F_{1,52}=8.19$, $P=0.0061$), but not of treatment ($F_{1,52}=2.45$, $P=0.1237$) and interaction ($F_{1,52}=0.87$, $P=0.3560$) in the PCtx (Fig. 4B–E). The Bonferroni post hoc test (NS vs. ST) found that long-term CIRS significantly increased the number of degenerating cells in L/V-Tg mice [$P<0.01$, in the DG (Fig. 4B); $P<0.05$, in the RCtx (Fig. 4D)]. Multiple comparisons with the Tukey–Kramer test found a significant increase in the number of degenerating neurons in the CA3 of the L/V-Tg(ST) mice [$P<0.0001$ vs. non-Tg(NS) and non-Tg(ST); $P<0.001$ vs. L/V-Tg(NS)] (Fig. 4C).

CIRS with pathogenic PS1 slightly affects the granule neuron precursors and proliferating cells

In stressed L/V-Tg mice, the number of degenerating neurons was significantly increased in the SGZ, where adult neurogenesis occurs. To examine the effect of stress with or without pathogenic PS1 on hippocampal neurogenesis, we next evaluated the number of Pax6+ in the hippocampus of L/V-Tg and non-Tg mice using our short-term CIRS protocol. Adult neurogenesis is an individualized, entire multi-step process but not a population event (Kempermann et al., 2004). Pax6, an essential transcription factor required for the production and maintenance of neural progenitor cells (Maekawa et al., 2005), is expressed in lineage-determined neuronal progenitors, differentiating granule neurons and bipotential (neural) precursor cells, and is strongly down-regulated during granule neuron differentiation (Nacher et al., 2005). In the adult hippocampal DG, proliferating granule neuron precursors that express GFAP and nestin molecules are always Pax6+ (Hevner et al., 2006; Maekawa et al., 2005; Nacher et al., 2005). Thus, Pax6 recently has been used as a suitable marker for newly generated cells (Osumi et al., 2008; von Bohlen Und Halbach, 2007; Winner et al., 2009). Whereas a small subpopulation of hilar mature neurons and certain astrocytes of the adult hippocampus express Pax6, Pax6+ cells in the SGZ are mostly granule neuron precursors (Nacher et al., 2005). Therefore, to evaluate the number of granule neuron precursors, we counted the cells expressing Pax6 localized in the SGZ where considerable new cell production occurs. We found that most Pax6+ cells were in the SGZ (Fig. 5A) and the number of these cells [% of non-Tg(NS)] tended to decrease in non-Tg (ST) and L/V-Tg(ST) mice (Fig. 5B). Yet, a two-way ANOVA revealed no significant effect of treatment ($F_{1,16}=2.04$, $P=0.1720$), genotype ($F_{1,16}=2.31$, $P=0.1479$), or interaction ($F_{1,16}=0.05$, $P=0.8203$). Consequently, we found that neither 3 weeks of CIRS (short-term) nor the PS1(L286V) genotype greatly affects the number of granule neuron precursors in the SGZ.

Granule neuron precursors are born in the SGZ and a neural precursor produces a bipotential neural cell and a lineage-determined neuronal cell through asymmetric division (Kempermann et al., 2004). We also measured the number of Ki-67+ cells per GCL to evaluate the proliferating cells. Ki-67 is present only in proliferating cells during G1, S, G2, and M, but not in the G0 phase of the cell cycle (Brown and Gatter, 1990; Kee et al., 2002). The number of Ki-67+ cells was subjected to a two-way ANOVA, which showed no significant effect of genotype [$F_{1,22}=0.18$, $P=0.6758$ (SGZ); $F_{1,22}=0.03$, $P=0.8705$ (hilus); $F_{1,22}=0.54$, $P=0.4710$ (GCL)], treatment [$F_{1,22}=0.61$, $P=0.4442$ (SGZ); $F_{1,22}=1.32$, $P=0.2631$ (hilus); $F_{1,22}=3.63$, $P=0.0700$ (GCL)], or interaction [$F_{1,22}=0.00$, $P=0.9901$ (SGZ); $F_{1,22}=0.60$, $P=0.4481$ (hilus); $F_{1,22}=0.12$, $P=0.7277$ (GCL)] (Fig. 5C). The percentage of Ki-67+ cells in the GCL and SGZ also

Fig. 4. The number of degenerating neurons is increased in the brains of stressed animals (long-term). (A) Silver-stained sections of mice exposed to chronic intermittent restraint stress (CIRS) (ST) or left untreated (NS). Scale bar, 100 μm. Inset shows boxed regions with higher magnification (scale bar, 10 μm). (B–E) Graphs indicate the number of degenerating neurons [expressed as % of non-Tg(NS), mean ± SEM] in the dentate gyrus (DG) (B), Cornus Ammonis 3 (CA3) (C), retrosplenial cortex (RCtx) (D), and piriform cortex (PCtx) (E). Statistical significance; DG (Bonferroni, NS vs. ST, @@$P<0.01$) (B); CA3 [Tukey–Kramer test, ***$P<0.0001$ vs. non-Tg(NS); ###$P<0.0001$ vs. non-Tg(ST); @@$P<0.001$ vs. L/V-Tg(NS)] (C); RCtx (Bonferroni, NS vs. ST, #$P<0.05$) (D). Non-Tg, transgenic negative mouse; L/V-Tg, transgenic mouse model of AD with overexpression of an FAD-type PS1; 23W, 23-week-old mice.

showed no significant effect of genotype ($F_{1,22}=0.05$, $P=0.8247$) or treatment ($F_{1,22}=3.84$, $P=0.0629$) or an interaction ($F_{1,22}=0.01$, $P=0.9205$). As a result, 3 weeks of CIRS slightly decreased the number of Ki-67+ proliferating cells in the SGZ, hilus, and GCL to a similar extent in non-Tg and L/V-Tg mice (Fig. 5C, D). In short, we confirmed that short-term CIRS primarily decreased the production of granule neuron precursors and the number of proliferating cells in the GCL and SGZ, yet the effect did not show significant differences between non-Tg and L/V-Tg backgrounds.

The impact of CIRS on newly synthesized cells lasts longer in Tg than in Non-Tg

In order to quantify the rate of neural production in the GCL and SGZ after stress exposure, we counted the newly synthesized cells by a single intraperitoneal injection of BrdU 20 h before perfusion. Unlike the measurement of the Pax6+ granule neuron precursors that integrates all of the marker-positive cells produced during the whole experimental (stressed/non-stressed) period, this BrdU labeling protocol can estimate only those cells newly synthesized within a day after stress cessation. When using Ki-67 to quantify the cell proliferation, newly generated cells that exit the cell cycle and enter their maturation process are not detected. BrdU is incorporated in cells at the S-phase, allowing us to detect both mitotic cells (Type-1, Type-2a, 2b, Type-3) and postmitotic cells (including late Type-3) in the hippocampal DG [the classification of the cellular stage in neurogenesis was performed in accordance with the review by Kempermann (Kempermann et al., 2004)] by immunohistochemical analyses using an anti-BrdU antibody. Actually, in adult hippocampal neurogenesis of mice, one can find a considerable number of cells labeled for both BrdU and NeuN (a post-mitotic, neuronal cell marker) even 1 day after a single injection of BrdU (Brandt et al., 2003). The number of BrdU+ cells in the GCL and SGZ [% of non-Tg(NS)] was subjected to a two-way ANOVA, and this analysis did show a significant effect of treatment ($F_{1,15}=24.12$, $P=0.0002$), but no effect of genotype ($F_{1,15}=2.06$, $P=0.1716$) and interaction ($F_{1,15}=1.78$, $P=0.2026$). Bonferroni *post hoc* tests (NS vs. ST) revealed that after CIRS, the number of BrdU+ cells was significantly reduced in L/V-Tg mice ($P<0.001$) [63 ± 7% of BrdU + cells in non-Tg(NS), Fig. 6A, B] but was not significantly decreased in non-Tg mice ($P>0.05$) [79 ± 9% of BrdU+ cells in non-Tg(NS), Fig. 6A, B]. This trend was almost parallel with the pattern in the body-weight-gain reductions (Supplementary Table 1). These results indicate that the impact of stress on newly synthesized cells in L/V-Tg mice lasted longer than that in non-Tg mice.

DCX+ neuronal progenitor cells increased after CIRS only in Tg

Although the significant reduction in the number of BrdU+ newly synthesized cells at 20 h after stress in L/V-Tg mice was apparent, the number of Pax6+ granule neuron precursors in the SGZ and Ki-67+ proliferating cells in the GCL and SGZ did not significantly decrease during the short-term CIRS. In hippocampal neurogenesis, a dividing precursor cell gives rise to daughter cells, which migrate away from the site of division and start to differentiate into neurons (Kempermann et al., 2004). We therefore evaluated the effect of short-term CIRS on the neuronal progenitor cells in the GCL and SGZ using the microtubule-associated protein doublecortin (DCX) as a marker. DCX is normally retained in cells within areas of continuous neurogenesis and expressed in mitotic and postmitotic cells (Brown et al., 2003; Couillard-Despres et al., 2005; Rao and Shetty, 2004), namely, proliferative nestin-positive neuronal progenitor cells (Type-2b), nestin-negative neuronal progenitor cells (Type-3), and postmitotic immature neurons that retain the vertical morphology with a rounded or slightly triangular nucleus and a clearly visible apical dendrite (late Type-3) (Kempermann et al., 2004). As the

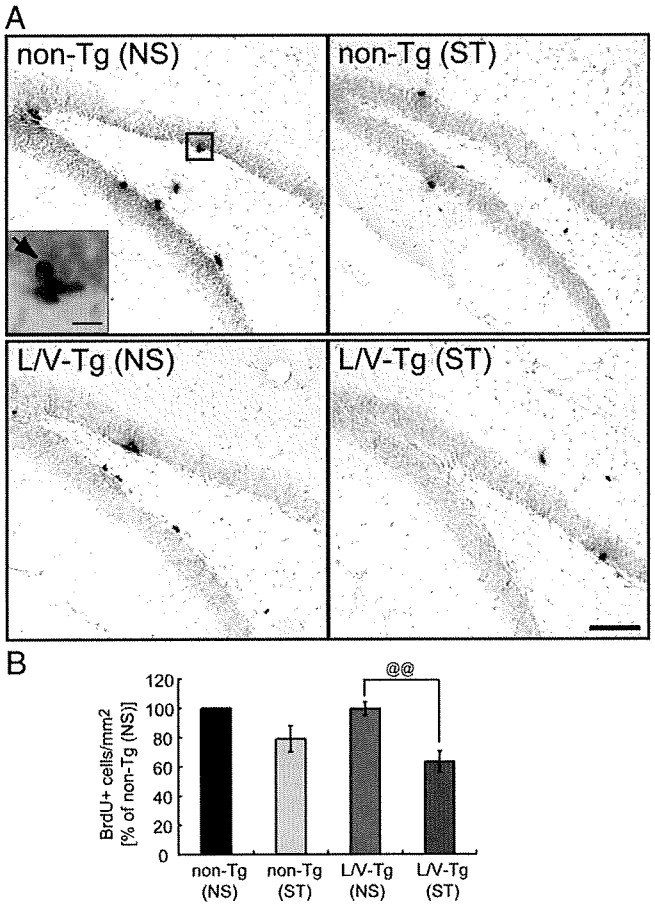

Fig. 6. The impact of chronic intermittent restraint stress (CIRS) on newly synthesized cells in the granule cell layer (GCL) and the subgranular zone (SGZ) lasts longer in L/V-Tg mice than in non-Tg mice. (A) Representative immunostaining of 5-bromo-2′-deoxyuridine (BrdU)+ cells. Scale bar, 50 μm. Inset shows boxed region with a higher magnification (scale bar, 10 μm). An arrow indicates a BrdU+ cell. (B) After CIRS, the number of BrdU+ cells in the GCL and SGZ [mean ± SEM, % of non-Tg(NS)] is significantly reduced in L/V-Tg mice (Bonferroni, NS vs. ST, @@$P<0.001$) but is not significantly decreased in non-Tg mice. Non-Tg, transgenic negative mouse; L/V-Tg, transgenic mouse model of AD with overexpression of an FAD-type PS1; NS, non-stressed control mice; ST, stressed mice.

newly generated cells began expressing mature neuronal markers, DCX immunoreactivity decreased sharply below the level of detection and remained undetectable thereafter (Brown et al., 2003; Couillard-Despres et al., 2005; Rao and Shetty, 2004). The number of DCX+ cells in the GCL and SGZ [% of non-Tg(NS)] was subjected to a two-way ANOVA, and this analysis showed a significant effect of treatment ($F_{1,30}=5.48$, $P=0.0261$) and an interaction ($F_{1,30}=23.37$, $P<0.0001$), but no effect of genotype ($F_{1,30}=1.76$, $P=0.1943$). Tukey-Kramer post hoc tests revealed significant differences in the number of DCX+ progenitor cells in the GCL and SGZ. In stressed non-Tg mice, the number of DCX+ cells significantly reduced [$P<0.0001$ vs. non-Tg(NS)] (Fig. 7A, B). This is in agreement with the trends observed for the Pax6+, Ki-67+, and BrdU+ cells. On the other hand, in L/V-Tg mice, the number of DCX+ cells was significantly reduced without stress [78 ± 2 % of DCX+ cells in non-Tg(NS); $P<0.0001$ vs. non-Tg(NS), Fig. 7B]. Unexpectedly, in L/V-Tg mice, the number of DCX+ neuronal progenitors was significantly increased by short-term CIRS [12 % increase compared with non-stressed L/V-Tg; $P<0.001$ vs. L/V-Tg(NS), Fig. 7B]. Equivalent data were obtained from confocal laser scanning microscopic analyses of the doublecortin (DCX)+ neuronal progenitor cells in the GCL and SGZ (Supplementary Fig. 4). Additionally, in the stressed L/V-Tg mice, the percentage of DCX+ cells that possessed long neurites (late

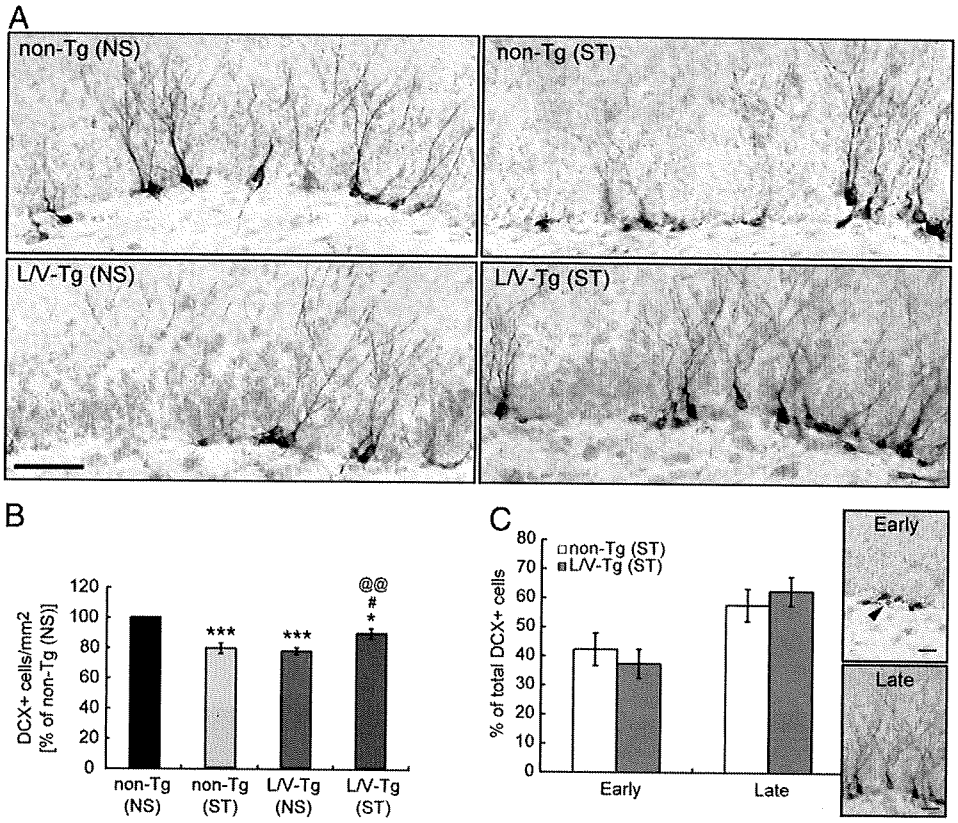

Fig. 7. Neuronal progenitor cells in the granule cell layer (GCL) and the subgranular zone (SGZ) increase after chronic intermittent restraint stress (CIRS) only in Tg. (A) Representative immunostaining of the doublecortin (DCX)+ neuronal progenitor cells in the GCL and SGZ. Scale bar, 50 μm. (B) The DCX+ cells in the GCL and SGZ [mean ± SEM, % of non-Tg(NS)] are significantly reduced in non-stressed L/V-Tg mice and are increased in stressed L/V-Tg mice. *P<0.05, ***P<0.0001 vs. non-Tg(NS); #P<0.05 vs. non-Tg(ST); @@P<0.001 vs. L/V-Tg(NS) (Tukey–Kramer test). (C) The percentage of DCX+ cells that possessed short neurites (Early, early progenitor cells) or long neurites (Late, late progenitor cells) in non-Tg(ST) and L/V-Tg(ST) mice (mean ± SEM). Scale bar, 50 μm. DCX+ late progenitor cells are modestly increased in L/V-Tg(ST) mice compared with non-Tg(ST) mice. Non-Tg, transgenic negative mouse; L/V-Tg, transgenic mouse model of AD with overexpression of an FAD-type PS1; NS, non-stressed control mice; ST, stressed mice.

progenitor cells) was modestly increased over that of non-Tg mice, whereas early progenitor cells tended to decrease compared with that of non-Tg mice (Fig. 7C).

Discussion

Our study indicates how gene–environment interaction affects adult neurogenesis in the hippocampal DG and deteriorates selective neurodegeneration in the neuronal circuit involved in cognitive function. We speculate that, in genetically predisposed animals, accumulated effects of subtle daily stresses such as metabolic oxidation may cause neurodegeneration, even in the absence of environmental stress.

Cellular and molecular machineries that accelerate neurodegeneration by chronic stress

Neurodegeneration in stressed L/V-Tg mice was more severe than in stressed non-Tg mice (Fig. 3). This might be due to increased vulnerability at the cellular or system levels, which is supported by our observation of abnormal calcium homeostasis in primary cultured hippocampal neurons prepared from neonatal L/V-Tg mice (data not shown). A previous report indicated that the PS1(L286V) mutation lowers the threshold to neurotoxicity through the disruption of calcium homeostasis and increased free radical production (Grilli et al., 2000; Guo et al., 1997). While structural changes after stress are often found in the CA3 (Conrad, 2006), we found that neurodegeneration in the stressed L/V-Tg mice was most prominent in the SGZ of the DG, where adult neurogenesis occurs. Because PS1 plays a role in neurogenesis both during development and in the adult (Wen et al., 2002), neurogenesis in the SGZ could be affected by chronic stress more than that in non-Tg mice.

In L/V-Tg mice, the number of DCX+ neuronal progenitors in the GCL and SGZ was significantly reduced without stress (Fig. 7A, B). This is in accord with recent evidence demonstrating that an FAD-related homozygous PS1 P264L mutation resulted in decreased numbers of DCX+ cells in the GCL (Zhang et al., 2007). On the other hand, the number of DCX+ cells in the GCL was significantly increased by short-term CIRS (Fig. 7A, B), which is consistent with the observation that the number of DCX+ cells in the hippocampal GCL increases in a senile cohort of AD patients (Jin et al., 2004). Another recent publication shows that increased proliferating cells in the presenile AD hippocampus are mostly accounted for by glial and vascular-associated changes, but not by neurogenesis (Boekhoorn et al., 2006). These contradictions can be attributed to multiple factors, such as different phases of AD progression, animal models, methodologies, and analytical tools (Kuhn et al., 2007). In our study, both decreased and increased states of DCX+ cells were driven in the L/V-Tg mice using the chronic stress model. These mice would therefore contribute to unravelling the aberrant neurogenic/nonneurogenic mechanisms that are part of the pathological events of neurodegenerative diseases.

Despite increased numbers of DCX+ cells in the GCL of AD patients (Jin et al., 2004) and short-term chronically stressed L/V-Tg mice, progressive neurodegeneration was still observed after long-term CIRS, implicating that the repair capacity of the DCX+ cells in the GCL is limited. Notably, the number of BrdU+ newly synthesized cells was significantly reduced in the GCL and SGZ (Fig. 6A, B). Considering the fact that BrdU+ cells contain both neural and neuronal fate cells (Maekawa et al., 2005), together with the observation that production of Pax6+ granule neuron precursors in the SGZ reached a similar

extent in stressed non-Tg and L/V-Tg mice, cells with a neuronal fate might preferentially be reduced in 20 h after CIRS. In stressed L/V-Tg mice, percentage of postmitotic DCX+ cells possessing longer neurites (late Type-3) was modestly increased compared with that in non-Tg (ST) mice, whereas the number of mitotic DCX+ cells (Type-2b and early Type-3) tended to decrease compared with that of non-Tg(ST) mice (Fig. 7C). This indicates that numerous DCX+ neuronal progenitor cells observed in the GCL and SGZ of stressed L/V-Tg mice were late-stage (posmitotic late Type-3), rather than early-stage (mitotic Type-2b and Type-3), in neuronal maturation. Collectively, these data suggest that an interaction between pathogenic PS1 and CIRS does affect neurogenesis during postmitotic neuronal cell maturation. We reasoned that the elevated number of DCX+ cells in the GCL and SGZ of stressed L/V-Tg mice was derived from an accumulation of immature neuronal progenitor cells rather than a replenishment of granule cells. A recent report indicated that DCX molecule supports dendritic arborization (Cohen et al., 2008). Given that DCX+ cells were accumulated in the GCL of stressed L/V-Tg mice, abnormal DCX degradation and consequent excessive stabilization of microtubules by DCX could in part explain the retardation of neuronal maturation and the resultant neurodegeneration. PS1 mutations might synergistically affect the expression, processing, or trafficking of molecules essential to neuronal maturation, such as Wnts, BDNF, and Trk receptors (Naruse et al., 1998), although further molecular–cellular assessment would be needed.

From a therapeutic point of view, it is necessary to elucidate the detailed molecular machinery that perturbs granule cell maturation and neurodegeneration in the hippocampal DG. The ability to recover from stress-related impaired neurogenesis, which was shown in wild-type adult rats (Heine et al., 2004), would be unbalanced presumably by the vulnerability derived from the mutated gene–chronic stress interaction in stressed L/V-Tg mice. For instance, under the stressed condition, apoptosis machinery is not available in L/V-Tg mice to actively eliminate those cells in abnormal neuronal differentiation, resulting in an accumulation of ill-balanced neurodegenerative cells in the hippocampus, even at the younger stages. This is partly supported by our observation that the number of TUNEL-positive apoptotic cells in the GCL did not significantly fluctuate between L/V-Tg and wild-type mice with CIRS (Supplementary Fig. 5), and the phenotype might further be strengthened by the fact that the number of newly synthesized cells assessed by BrdU was 33% decreased in L/V-Tg(ST) mice (Fig. 6). A non-cell autonomous microenvironmental niche induced by FAD-linked PS1 variants could be additionally responsible for the impaired neurogenesis and neurodegeneration (Choi et al., 2008).

Conclusions

Our results suggest that, in individuals predisposed to genetic mutations for AD, stress accelerates the inhibition of neuronal maturation, thereby enhancing neurodegenerative vulnerability that depends on mutated gene–environment interaction. Chronically stressed L/V-Tg mice could be useful animal models to elucidate the key molecular machinery and therapeutic targets for AD. Our experimental strategy using controlled stress should provide insights into the pathogenic mechanisms of AD as well as other neurodegenerative diseases.

Acknowledgments

We thank Drs. S. Kohsaka and M. Hoshino for their help, Ms. T. Kohno and J. Asami for technical assistance and all other members of the Shindan, DDND and DVDR lab for fruitful discussions. We also thank Drs. H. Kumanogoh, R. Setsuie, K. Zushida, T. Maruoka, M. Yokosuka, K. Yuyama, T. Kikusui, and K. Moriya for providing useful information. This work was supported by a Grant-in-Aid for Young Scientists (B) (#18790607; #21790639) to S.K., grants from Research Foundation ITSUU Laboratory and Takeda Science Foundation to T.I., and the Program for Promotion of Fundamental Studies in Health Sciences of the National Institute of Biomedical Innovation (05-32) to S. N., K. W. and T. I.

Appendix A. Supplementary data

Supplementary data associated with this article can be found, in the online version, at doi:10.1016/j.expneurol.2009.10.020.

References

Boekhoorn, K., Joels, M., Lucassen, P.J., 2006. Increased proliferation reflects glial and vascular-associated changes, but not neurogenesis in the presenile Alzheimer hippocampus. Neurobiol. Dis. 24, 1–14.
Brandt, M.D., Jessberger, S., Steiner, B., Kronenberg, G., Reuter, K., Bick-Sander, A., von der Behrens, W., Kempermann, G., 2003. Transient calretinin expression defines early postmitotic step of neuronal differentiation in adult hippocampal neurogenesis of mice. Mol. Cell. Neurosci. 24, 603–613.
Brown, D.C., Gatter, K.C., 1990. Monoclonal antibody Ki-67: its use in histopathology. Histopathology 17, 489–503.
Brown, J.P., Couillard-Després, S., Cooper-Kuhn, C.M., Winkler, J., Aigner, L., Kuhn, H.G., 2003. Transient expression of doublecortin during adult neurogenesis. J. Comp. Neurol. 467, 1–10.
Bruel-Jungerman, E., Laroche, S., Rampon, C., 2005. New neurons in the dentate gyrus are involved in the expression of enhanced long-term memory following environmental enrichment. Eur. J. Neurosci. 21, 513–521.
Buckner, R.L., 2004. Memory and executive function in aging and AD: multiple factors that cause decline and reserve factors that compensate. Neuron 44, 195–208.
Cameron, H.A., McKay, R.D., 2001. Adult neurogenesis produces a large pool of new granule cells in the dentate gyrus. J. Comp. Neurol. 435, 406–417.
Choi, S.H., Veeraraghavalu, K., Lazarov, O., Marler, S., Ransohoff, R.M., Ramirez, J.M., Sisodia, S.S., 2008. Non-cell-autonomous effects of presenilin 1 variants on enrichment-mediated hippocampal progenitor cell proliferation and differentiation. Neuron 59, 568–580.
Chui, D.H., Tanahashi, H., Ozawa, K., Ikeda, S., Checler, F., Ueda, O., Suzuki, H., Araki, W., Inoue, H., Shirotani, K., Takahashi, K., Gallyas, F., Tabira, T., 1999. Transgenic mice with Alzheimer presenilin 1 mutations show accelerated neurodegeneration without amyloid plaque formation. Nat. Med. 5, 560–564.
Cohen, D., Segal, M., Reiner, O., 2008. Doublecortin supports the development of dendritic arbors in primary hippocampal neurons. Dev. Neurosci. 30, 187–199.
Conrad, C.D., 2006. What is the functional significance of chronic stress-induced CA3 dendritic retraction within the hippocampus? Behav. Cogn. Neurosci. Rev. 5, 41–60.
Couillard-Despres, S., Winner, B., Schaubeck, S., Aigner, R., Vroemen, M., Weidner, N., Bogdahn, U., Winkler, J., Kuhn, H.G., Aigner, L., 2005. Doublecortin expression levels in adult brain reflect neurogenesis. Eur. J. Neurosci. 21, 1–14.
Drapeau, E., Mayo, W., Aurousseau, C., Le Moal, M., Piazza, P.V., Abrous, D.N., 2003. Spatial memory performances of aged rats in the water maze predict levels of hippocampal neurogenesis. Proc. Natl. Acad. Sci. U. S. A. 100, 14385–14390.
Golde, T.E., Eckman, C.B., Younkin, S.G., 2000. Biochemical detection of Abeta isoforms: implications for pathogenesis, diagnosis, and treatment of Alzheimer's disease. Biochim. Biophys. Acta 1502, 172–187.
Gould, E., Tanapat, P., 1999. Stress and hippocampal neurogenesis. Biol. Psychiatry 46, 1472–1479.
Gould, E., Beylin, A., Tanapat, P., Reeves, A., Shors, T.J., 1999. Learning enhances adult neurogenesis in the hippocampal formation. Nat. Neurosci. 2, 260–265.
Grilli, M., Diodato, E., Lozza, G., Brusa, R., Casarini, M., Uberti, D., Rozmahel, R., Westaway, D., St George-Hyslop, P., Memo, M., Ongini, E., 2000. Presenilin-1 regulates the neuronal threshold to excitotoxicity both physiologically and pathologically. Proc. Natl. Acad. Sci. U. S. A. 97, 12822–12827.
Guo, Q., Sopher, B.L., Furukawa, K., Pham, D.G., Robinson, N., Martin, G.M., Mattson, M.P., 1997. Alzheimer's presenilin mutation sensitizes neural cells to apoptosis induced by trophic factor withdrawal and amyloid beta-peptide: involvement of calcium and oxyradicals. J. Neurosci. 17, 4212–4222.
Heine, V.M., Maslam, S., Zareno, J., Joëls, M., Lucassen, P.J., 2004. Suppressed proliferation and apoptotic changes in the rat dentate gyrus after acute and chronic stress are reversible. Eur. J. Neurosci. 19, 131–144.
Hevner, R.F., Hodge, R.D., Daza, R.A., Englund, C., 2006. Transcription factors in glutamatergic neurogenesis: conserved programs in neocortex, cerebellum, and adult hippocampus. Neurosci. Res. 55, 223–233.
Imayoshi, I., Sakamoto, M., Ohtsuka, T., Takao, K., Miyakawa, T., Yamaguchi, M., Mori, K., Ikeda, T., Itohara, S., Kageyama, R., 2008. Roles of continuous neurogenesis in the structural and functional integrity of the adult forebrain. Nat. Neurosci. 11, 1153–1161.
Ino, H., 2003. Antigen retrieval by heating en bloc for pre-fixed frozen material. J. Histochem. Cytochem. 51, 995–1003.
Inoue, T., Nakamura, S., Osumi, N., 2000. Fate mapping of the mouse prosencephalic neural plate. Dev. Biol. 219, 373–383.
Jack Jr., C.R., Petersen, R.C., O'Brien, P.C., Tangalos, E.G., 1992. MR-based hippocampal volumetry in the diagnosis of Alzheimer's disease. Neurology 42, 183–188.
Jeong, Y.H., Park, C.H., Yoo, J., Shin, K.Y., Ahn, S.M., Kim, H.S., Lee, S.H., Emson, P.C., Suh, Y.H., 2006. Chronic stress accelerates learning and memory impairments and increases

amyloid deposition in APPV717I-CT100 transgenic mice, an Alzheimer's disease model. FASEB J. 20, 729–731.
Jin, K., Peel, A.L., Mao, X.O., Xie, L., Cottrell, B.A., Henshall, D.C., Greenberg, D.A., 2004. Increased hippocampal neurogenesis in Alzheimer's disease. Proc. Natl. Acad. Sci. U. S. A. 101, 343–347.
Kee, N., Sivalingam, S., Boonstra, R., Wojtowicz, J.M., 2002. The utility of Ki-67 and BrdU as proliferative markers of adult neurogenesis. J. Neurosci. Methods 115, 97–105.
Kempermann, G., Gage, F.H., 2002. Genetic determinants of adult hippocampal neurogenesis correlate with acquisition, but not probe trial performance, in the water maze task. Eur. J. Neurosci. 16, 129–136.
Kempermann, G., Jessberger, S., Steiner, B., Kronenberg, G., 2004. Milestones of neuronal development in the adult hippocampus. Trends Neurosci. 27, 447–452.
Killiany, R.J., Moss, M.B., Albert, M.S., Sandor, T., Tieman, J., Jolesz, F., 1993. Temporal lobe regions on magnetic resonance imaging identify patients with early Alzheimer's disease. Arch. Neurol. 50, 949–954.
Kim, K.S., Han, P.L., 2006. Optimization of chronic stress paradigms using anxiety- and depression-like behavioral parameters. J. Neurosci. Res. 83, 497–507.
Kuhn, H.G., Cooper-Kuhn, C.M., Boekhoorn, K., Lucassen, P.J., 2007. Changes in neurogenesis in dementia and Alzheimer mouse models: are they functionally relevant? Eur. Arch. Psychiatry Clin. Neurosci. 257, 281–289.
Maekawa, M., Takashima, N., Arai, Y., Nomura, T., Inokuchi, K., Yuasa, S., Osumi, N., 2005. Pax6 is required for production and maintenance of progenitor cells in postnatal hippocampal neurogenesis. Genes Cells 10, 1001–1014.
Masters, C.L., Beyreuther, K., 1998. Alzheimer's disease. British Med. J. 316, 446–448.
Mattson, M.P., 2004. Pathways towards and away from Alzheimer's disease. Nature 430, 631–639.
Nacher, J., Varea, E., Blasco-Ibañez, J.M., Castillo-Gomez, E., Crespo, C., Martinez-Guijarro, F.J., McEwen, B.S., 2005. Expression of the transcription factor Pax 6 in the adult rat dentate gyrus. J. Neurosci. Res. 81, 753–761.
Nagata, K., Nakashima-Kamimura, N., Mikami, T., Ohsawa, I., Ohta, S., 2009. Consumption of molecular hydrogen prevents the stress-induced impairments in hippocampus-dependent learning tasks during chronic physical restraint in mice. Neuropsychopharmacology 34, 501–508.
Naruse, S., Thinakaran, G., Luo, J.J., Kusiak, J.W., Tomita, T., Iwatsubo, T., Qian, X., Ginty, D.D., Price, D.L., Borchelt, D.R., Wong, P.C., Sisodia, S.S., 1998. Effects of PS1 deficiency on membrane protein trafficking in neurons. Neuron 21, 1213–1221.
Ogita, K., Nishiyama, N., Sugiyama, C., Higuchi, K., Yoneyama, M., Yoneda, Y., 2005. Regeneration of granule neurons after lesioning of hippocampal dentate gyrus: evaluation using adult mice treated with trimethyltin chloride as a model. J. Neurosci. Res. 82, 609–621.
Osumi, N., Shinohara, H., Numayama-Tsuruta, K., Maekawa, M., 2008. Concise review: Pax6 transcription factor contributes to both embryonic and adult neurogenesis as a multifunctional regulator. Stem Cells 26, 1663–1672.
Pardon, M.C., Rattray, I., 2008. What do we know about the long-term consequences of stress on ageing and the progression of age-related neurodegenerative disorders? Neurosci. Biobehav. Rev. 32, 1103–1120.
Paxinos, G., Franklin, K.B., 2001. The Mouse Brain in Stereotaxic Coordinates, 2nd edn. Academic Press, San Diego.
Rao, M.S., Shetty, A.K., 2004. Efficacy of doublecortin as a marker to analyse the absolute number and dendritic growth of newly generated neurons in the adult dentate gyrus. Eur. J. Neurosci. 19, 234–246.
Rosenbrock, H., Koros, E., Bloching, A., Podhorna, J., Borsini, F., 2005. Effect of chronic intermittent restraint stress on hippocampal expression of marker proteins for synaptic plasticity and progenitor cell proliferation in rats. Brain Res. 1040, 55–63.
Sandi, C., 2004. Stress, cognitive impairment and cell adhesion molecules. Nat. Rev. Neurosci. 5, 917–930.
Shors, T.J., Miesegaes, G., Beylin, A., Zhao, M., Rydel, T., Gould, E., 2001. Neurogenesis in the adult is involved in the formation of trace memories. Nature 410, 372–376.
Veena, J., Srikumar, B.N., Mahati, K., Bhagya, V., Raju, T.R., Shankaranarayana Rao, B.S., 2009. Enriched environment restores hippocampal cell proliferation and ameliorates cognitive deficits in chronically stressed rats. J. Neurosci. Res. 87, 831–843.
von Bohlen Und Halbach, O., 2007. Immunohistological markers for staging neurogenesis in adult hippocampus. Cell Tissue Res. 329, 409–420.
Wen, P.H., Friedrich Jr., V.L., Shioi, J., Robakis, N.K., Elder, G.A., 2002. Presenilin-1 is expressed in neural progenitor cells in the hippocampus of adult mice. Neurosci. Lett. 318, 53–56.
Winner, B., Desplats, P., Hagl, C., Klucken, J., Aigner, R., Ploetz, S., Laemke, J., Karl, A., Aigner, L., Masliah, E., Buerger, E., Winkler, J., 2009. Dopamine receptor activation promotes adult neurogenesis in an acute Parkinson model. Exp. Neurol. 219, 543–552.
Zhang, C.L., Zou, Y., He, W., Gage, F.H., Evans, R.M., 2008. A role for adult TLX-positive neural stem cells in learning and behaviour. Nature 451, 1004–1007.
Zhang, C., McNeil, E., Dressler, L., Siman, R., 2007. Long-lasting impairment in hippocampal neurogenesis associated with amyloid deposition in a knock-in mouse model of familial Alzheimer's disease. Exp. Neurol. 204, 77–87.

Visualization of ATP levels inside single living cells with fluorescence resonance energy transfer-based genetically encoded indicators

Hiromi Imamura[a,b,1], Kim P. Huynh Nhat[b], Hiroko Togawa[b], Kenta Saito[c], Ryota Iino[b], Yasuyuki Kato-Yamada[d], Takeharu Nagai[a,c], and Hiroyuki Noji[b,1]

[a]Precursory Research for Embryonic Science, Japan Science and Technology Agency, 5 Sanbancho, Chiyoda-ku, Tokyo 102-0075, Japan; [b]Institute of Scientific and Industrial Research, Osaka University, 8-1 Mihogaoka, Ibaraki, Osaka 567-0047, Japan; [c]Research Institute for Electronic Science, Hokkaido University, Kita-20 Nishi-10, Kita-ku, Sapporo, Hokkaido 001-0020, Japan; and [d]Department of Life Science, Rikkyo University, 3-34-1 Nishi-Ikebukuro, Toshima-ku, Tokyo 171-8501, Japan

Edited by James A. Wells, University of California, San Francisco, CA, and approved July 29, 2009 (received for review April 30, 2009)

Adenosine 5′-triphosphate (ATP) is the major energy currency of cells and is involved in many cellular processes. However, there is no method for real-time monitoring of ATP levels inside individual living cells. To visualize ATP levels, we generated a series of fluorescence resonance energy transfer (FRET)-based indicators for ATP that were composed of the ε subunit of the bacterial F_oF_1-ATP synthase sandwiched by the cyan- and yellow-fluorescent proteins. The indicators, named ATeams, had apparent dissociation constants for ATP ranging from 7.4 μM to 3.3 mM. By targeting ATeams to different subcellular compartments, we unexpectedly found that ATP levels in the mitochondrial matrix of HeLa cells are significantly lower than those of cytoplasm and nucleus. We also succeeded in measuring changes in the ATP level inside single HeLa cells after treatment with inhibitors of glycolysis and/or oxidative phosphorylation, revealing that glycolysis is the major ATP-generating pathway of the cells grown in glucose-rich medium. This was also confirmed by an experiment using oligomycin A, an inhibitor of F_oF_1-ATP synthase. In addition, it was demonstrated that HeLa cells change ATP-generating pathway in response to changes of nutrition in the environment.

fluorescent indicator | FRET | live imaging | oxidative phosphorylation

Adenosine 5′-triphosphate (ATP) is the ubiquitous energy currency of all living organisms. The high phosphate-transfer potential of ATP is used for many biological processes, including muscle contraction, synthesis and degradation of biological molecules, and membrane transport. In addition, it has been suggested that ATP acts as an intracellular or extracellular signaling molecule in cellular processes, such as insulin secretion (1), neurotransmission (2), cell motility (3), and organ development (4). However, it has been difficult to precisely understand how ATP controls cellular processes and how the intracellular ATP level is regulated at the single cell level, because the conventional ATP quantification methods can only provide the averaged ATP level of an ensemble of cells based on cell extract analysis. Moreover, the distribution pattern of ATP between different intracellular compartments is unclear. Several attempts have been made to monitor ATP levels real-time in individual cells; however, these methods present several problems. For example, in chemiluminescence imaging from cells expressing firefly luciferase (5), chemiluminescence by luciferase depends not only on the intracellular ATP level but also on the luciferase concentration, as well as the other substrates, oxygen, and luciferin. Moreover, pH also affects luciferase activity. Another drawback of this method is that the intracellular ATP level could be perturbed because of ATP consumption. Furthermore, the dim luminescence of luciferase requires longer exposure time for image acquisition, making real-time observation cumbersome. Other approaches include measurement of the ion channel activity (6) or conformational change (7) of the ATP-sensitive potassium channel (K_{ATP} channel). These methods are limited to measurements of regions around the plasma membrane. In addition, K_{ATP} channel expression may also affect the characteristics of cells. Recently, a fluorescent indicator of the ATP:ADP ratio was developed (8). Although this probe is suitable for monitoring the cellular energy level, it cannot be used to directly measure the ATP level.

Here, we report on genetically-encoded fluorescence resonance energy transfer (FRET)-based ATP indicators that employ the ε subunit of the bacterial F_oF_1-ATP synthase. By using these indicators, the ATP levels in different cellular compartments and the dynamics of ATP in real-time can be monitored at the single cell level. The bacterial ε subunit is one of the smallest ATP-binding proteins (14 kDa), which is composed of one N-terminal β-barrel domain and two C-terminal α-helices (Fig. 1). The physiological role of the ε subunit is thought to be the regulation of the F_oF_1-ATP synthase activity depending on the intracellular ATP level (9–11). The ε subunit confers several advantages for a FRET-based ATP sensor. One is that the ε subunit binds to ATP, but does not hydrolyze it. Another advantageous feature of the ε subunit is the very high specificity for ATP over the other nucleotides; ADP, GTP, CTP, and UTP (12). Furthermore, the ε subunit undergoes a large conformational change into a folded form upon ATP binding, by bundling the two α-helices, which are relaxed in the absence of ATP (13, 14) (Fig. 2*A*). This large conformational change upon ATP binding may ensures a large dynamic range of the FRET signal.

Results

Development of a Series of ATP Indicators. We invented a FRET-based ATP indicator by genetically linking mseCFP (15)—a variant of cyan fluorescent protein (CFP)—with monomeric (A206K) Venus (mVenus) (16, 17)—a variant of yellow fluorescent protein (YFP)—each at either the N- or C terminus of the ε subunit, which was derived from *Bacillus subtilis* F_oF_1-ATP synthase. The generated indicator was termed ATeam (Adenosine 5′-Triphosphate indicator based on Epsilon subunit for Analytical Measurements). Four hydrophobic amino acid residues (Val-9, Leu-42, Phe-67, and Leu-78) forming a hydrophobic surface to interact with the F_oF_1 complex were replaced by

Author contributions: H.I. and H.N. designed research; H.I., K.P.H.N., H.T., K.S., and T.N. performed research; R.I., Y.K.-Y., and T.N. contributed new reagents/analytic tools; H.I., K.P.H.N., H.T., K.S., and T.N. analyzed data; and H.I. and H.N. wrote the paper.

The authors declare no conflict of interest.

This article is a PNAS Direct Submission.

Freely available online through the PNAS open access option.

[1]To whom correspondence may be addressed. E-mail: imamura@sanken.osaka-u.ac.jp or hnoji@sanken.osaka-u.ac.jp.

This article contains supporting information online at www.pnas.org/cgi/content/full/0904764106/DCSupplemental.

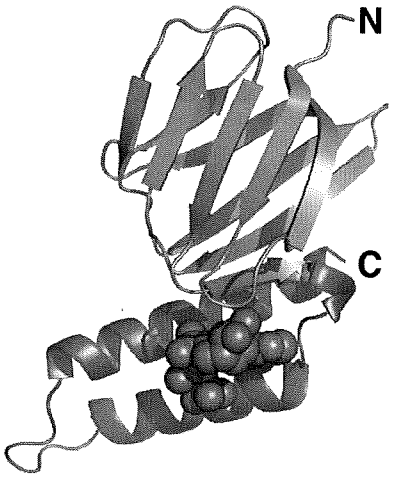

Fig. 1. Three-dimensional structure of *Bacillus* sp. PS3 ε subunit complexed with ATP (14). The N-terminal β-sandwich domain (residues 1–84) and C-terminal α-helical domain (residues 85–133) are colored green and magenta, respectively. ATP is represented as a cyan sphere model.

hydrophilic residues, to retard incorporation into the F_oF_1 and reduce nonspecific hydrophobic interaction with other proteins. The dynamic range of FRET signal of the initial construct was not considerably large (data not shown). It has been demonstrated that by altering the relative orientations between donor and acceptor fluorescent proteins of a cameleon calcium indicator using a circularly permuted fluorescent protein, dynamic range of FRET signal can be efficiently enhanced (18). To improve the dynamic range of the ATeam, we substituted the mVenus part of the ATeam with several circularly permuted mVenus (18). A circularly permuted mVenus having the 173rd amino acid as its N terminus (cp173-mVenus) yielded the largest dynamic range; the construct is termed AT1.03 (Fig. 2*A* and Fig. S1). The FRET signal increased by ≈2.3-fold (as assessed by the emission ratio of 527/475 nm) upon the addition of ATP in vitro (Fig. 2*B*). The dissociation constant (K_d) of AT1.03 was determined as 3.3 mM at 37 °C from plots of the emission ratio against ATP concentration (here after [ATP]) (Fig. 2*C*). Thus, AT1.03 can be used for measuring intracellular ATP levels in the millimolar range. To develop an indicator with higher affinity, we constructed an ATeam employing the ε subunit of *Bacillus* sp. PS3, termed AT3.10 (Fig. S1), on the basis of the findings of previous studies, wherein the isolated ε subunit derived from the thermophilic *Bacillus* sp. PS3 was shown to exhibit ≈500-fold higher affinity to ATP than that derived from mesophilic *B. subtilis* (19, 20). As expected, the fluorescence emission ratio of AT3.10 changed at significantly lower [ATP] than AT1.03, and the apparent K_d of AT3.10 was determined to be 7.4 μM at 37 °C (Fig. 2*C*). It is unclear why the affinity between the two ε subunits differs markedly, despite the high similarity of amino acid sequences (≈70% identity) and high conservation of the amino acid residues that directly interact with ATP (Fig. S2*A*). We found that the 60th residue in the N-terminal β-sandwich domain and the 132nd residue in the C-terminal α-helical domain, which closely interact in the crystal structure of the ATP-bound form of *Bacillus* sp. PS3 ε subunit, are not conserved between the two ε subunits (Fig. S2). Residues adjacent to the 132nd residue that do not have direct interaction with ATP are also not conserved. Expecting that these residues might contribute to the affinity of the ε subunit, these residues were exchanged between AT1.03 and AT3.10 to construct $AT1.03^{YEMK}$ and $AT3.10^{MGK}$ (Fig. S1). The apparent K_d values of $AT1.03^{YEMK}$ and $AT3.10^{MGK}$ were 1.2 mM and 14 μM at 37 °C (Fig. 2*C*), which is approximately three-fold less and two-fold more than that of the original constructs. These results indicate that the affinity of the ε subunit is partly determined by the stability of the folded form, and that the affinity of the ATeam to ATP can be adjusted to conduct individual experiments, by simply substituting the ε subunit with that of a different bacteria and/or by introducing point mutations into the interface between the N- and C-terminal domains of the ε subunit.

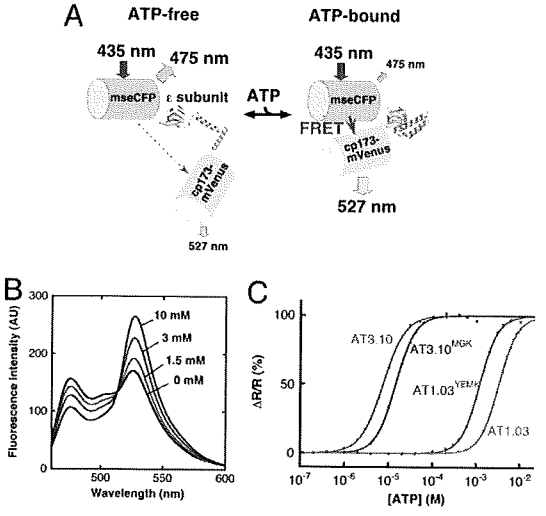

Fig. 2. FRET-based ATP probes, ATeam. (*A*) Schematic drawing of AT1.03 probe. Variants of CFP (mseCFP) and YFP (cp173-mVenus) were connected by the ε subunit of *Bacillus subtilis* F_oF_1-ATP synthase. In the ATP-free form (left), extended and flexible conformations of the ε subunit separate the two fluorescent proteins, resulting in low FRET efficiency. In the ATP-bound form, the ε subunit retracts to draw the two fluorescent proteins close to each other, which increases FRET efficiency. (*B*) ATP-dependent fluorescence spectral change of AT1.03 in vitro. Fluorescence emission of AT1.03 proteins at various ATP concentrations ([ATP]) and at 37 °C in 50 mM Mops-KOH (pH 7.3), 50 mM KCl, 0.5 mM $MgCl_2$, and 0.05% Triton X-100 was measured by exciting with 435 nm light. (*C*) ATP-dependent fluorescence emission ratio (R) changes of four ATeam proteins in vitro. The fraction of emission ratio (527/475 nm) change was plotted against [ATP]. Fluorescence of ATeam proteins was measured as in (*B*). Plots were fitted using a Hill equation: $\Delta R/R = \Delta R \times [ATP]^n/([ATP]^n + K_d^n)$. The apparent dissociation constant (K_d) and Hill coefficient (n) were calculated to be 7.4 μM and 1.7 (AT3.10), 14 μM and 2.0 (AT3.10MGK), 1.2 mM and 2.1 (AT1.03YEMK), and 3.3 mM and 2.1 (AT1.03), respectively.

Characterization of ATeam Indicators In Vitro. We further examined the characteristics of the purified ATeam indicators in vitro. In contrast to the effect observed on ATP addition, addition of up to 10 mM GTP or ADP had little effect on the YFP/CFP emission ratio of AT1.03 (Fig. 3*A*), which was consistent with previous findings (19). We also found that addition of even dATP did not increase the emission ratio of AT1.03 (Fig. 3*A*); rather, the emission ratio gradually decreased for unknown reasons (≈10% decrease at 10 mM ADP). AT3.10 also exhibited high selectivity for ATP: it showed 30-fold and 300-fold lower affinity to ADP (K_d = 0.23 mM) and GTP (K_d = 2.6 mM), respectively (Fig. S3), also consistent with previous studies (12, 13). The pH dependence of the FRET signal of AT1.03 was also examined. The fluorescence emission ratio was almost invariant from pH 7.1 to 8.5 (Fig. 3*B*), suggesting that the fluorescence signal from AT1.03 will not be affected by small pH fluctuations around normal cytoplasmic pH, which is near 7.3 (21). The rates of ATP binding (k_{on}) and dissociation (k_{off}) were determined to be 1.7×10^{-2} mM^{-1} s^{-1} and 9.8×10^{-2} s^{-1}, respectively (Fig. 3*C*). Thus, AT1.03 can be used to monitor the dynamics of ATP changes with rates up to 0.1 s^{-1}. Further, the temperature

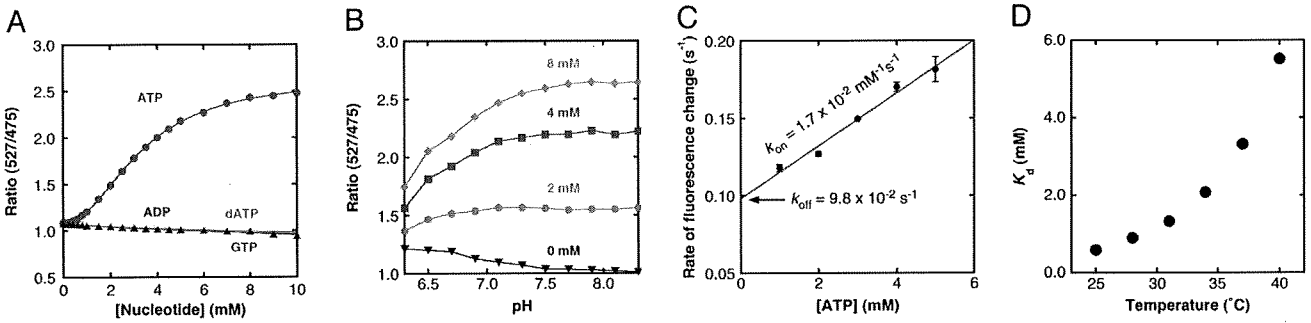

Fig. 3. Characterization of purified AT1.03 in vitro. (*A*) Nucleotide selectivity of AT1.03. The fluorescence emission ratio (527/475 nm) at 37 °C was plotted against nucleotide concentrations. Red filled circle, ATP; blue filled circle, ADP; green open square, GTP; orange open circle, dATP. Plots were fitted with Hill equations; $R = (R_{max} - R_{min}) \times [S]^n/([S]^n + K_d^n) + R_{min}$, where R_{max} and R_{min} are the maximum and minimum fluorescence ratios, respectively, K_d is the apparent dissociation constant, and n is a Hill coefficient. (*B*) pH dependence of AT1.03. The fluorescence ratios (527/475 nm) at 37 °C at 0, 2, 4, and 8 mM ATP in the pH range of 6.3–8.3 are shown. The buffer contained 50 mM Mops-KOH (pH 6.3–7.5) or Hepes-KOH (pH 7.7–8.3), 50 mM potassium chloride, 0.5 mM magnesium chloride, and 0.05% Triton X-100. (*C*) Reaction rate constants of AT1.03. Apparent rate constants ($k^{app} = k_{on}[ATP] + k_{off}$) at 37 °C, which were determined by fitting the CFP fluorescence decrease after ATP addition with a single exponential equation, were plotted against ATP concentrations ([ATP]). From a linear fit to the plot, k_{on} and k_{off} were calculated as 1.7×10^{-2} $mM^{-1}s^{-1}$ and 9.8×10^{-2} s^{-1}, respectively. (*D*) Dependence of K_d on temperature. K_d values for ATP were measured as in (*A*) at 25, 28, 31, 34, 37, and 40 °C.

dependence of the affinity was investigated (Fig. 3*D*): the dissociation constant of AT1.03 was elevated approximately five-fold by an increase of 10 °C, close to the temperature-sensitivity of the isolated *Bacillus* sp. PS3 ε subunit (13).

Comparison of ATP Levels in Different Subcellular Compartments. Next, we visualized the ATP levels inside subcellular compartments of single living HeLa cells expressing AT1.03 for the investigation of ATP distribution among cellular compartments. When AT1.03 without a targeting sequence was expressed in HeLa cells, it was mainly distributed in the cytoplasm, and slightly in the nucleus (Fig. 4*A*). For the targeting ATeam into the nucleus or mitochondrial matrix, a triplet of the nuclear localization signal of SV40 large T-antigen or a duplex of the mitochondrial targeting signal of cytochrome *c* oxidase subunit VIII were each fused to the N terminus of AT1.03 (nucAT1.03 and mitAT1.03; Fig. S1). These indicators were properly localized to the desired cellular compartments (Fig. 4 *B* and *C*). The YFP/CFP emission ratio was calculated from CFP and YFP fluorescence images of the individual cells, which were recorded using a wide-field fluorescence microscope. We found that ATeam localized in the mitochondrial matrix showed a significantly lower YFP/CFP emission ratio than that in the cytoplasm or nucleus (Fig. 4). The nucleus also showed a lower YFP/CFP emission ratio than the cytoplasm, but to a smaller extent (Fig. 4*D*), suggesting that ATP can pass through nuclear pores almost freely. The mitochondrial targeting sequence will not affect the fluorescence ratio, because as demonstrated for the cameleon calcium indicator, the targeting sequence is cleaved after transport into mitochondria (22). Higher mitochondrial pH does not account for the lower YFP/CFP emission ratio, because the fluorescence of AT1.03 is almost invariant at pH conditions >7.3 (Fig. 3*B*). To confirm that the low YFP/CFP emission ratio in mitochondria is not due to some environmental effects but ATP level, HeLa cells expressing derivatives of AT1.03 with different affinity to ATP were also investigated. First, the same measurements were carried out using $AT1.03^{YEMK}$, which has a higher affinity as described above. Although the YFP/CFP emission ratio of mitochondria was lower than that of cytoplasm, their difference (16%) was much smaller than that (34%) observed with AT1.03 (Fig. 4*D*). This means that the FRET signal of cytoplasm is almost saturated. The nucleus showed the same ratio as cytoplasm also due to the saturation of the FRET signal. Then, we used another type of ATeam, which was designed not to response to ATP. Structural studies revealed that two arginine residues in the position of 122 and 126 of the ε subunit have a direct contact with the α and β phosphates of ATP (Fig. S4*A*), suggesting their crucial roles on the ATP recognition. A recent biochemical study showed that the substitution of these residues with other ones leads drastic decrement of the affinity to ATP (20). We constructed the

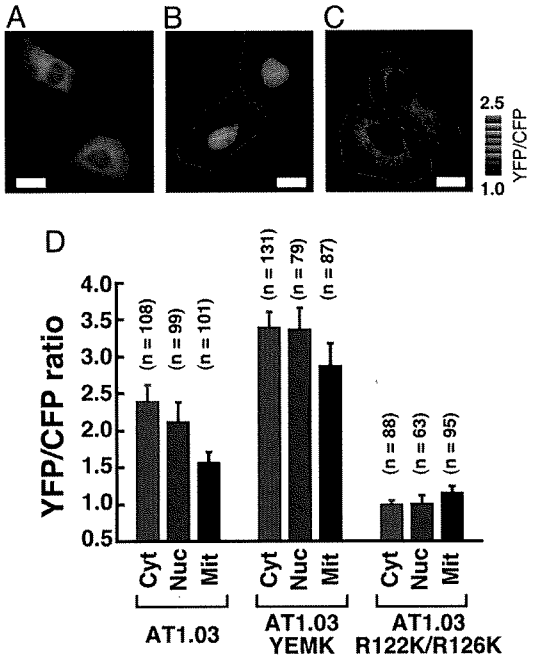

Fig. 4. Comparison of ATP concentrations ([ATP]) between different cellular compartments. (*A–C*) Expression of ATeam in different cellular compartments. Ratiometric pseudocolor images of AT1.03 expressed in cytoplasm (*A*), nucleus (*B*), and mitochondria (*C*) of HeLa cells. White lines represent cell outline. (Scale bar, 20 μm.) (*D*) Comparison of YFP/CFP emission ratio of ATeams in different cellular compartments. Three ATeams (AT1.03, $AT1.03^{YEMK}$, $AT1.03^{R122K/R126K}$), which have different affinity to ATP, were expressed in cytoplasm, nucleus, or mitochondria of HeLa cells. The ratio was calculated from fluorescent images. The numbers of cells used for calculating the ratio are indicated. Error bars are standard deviation of ratios.

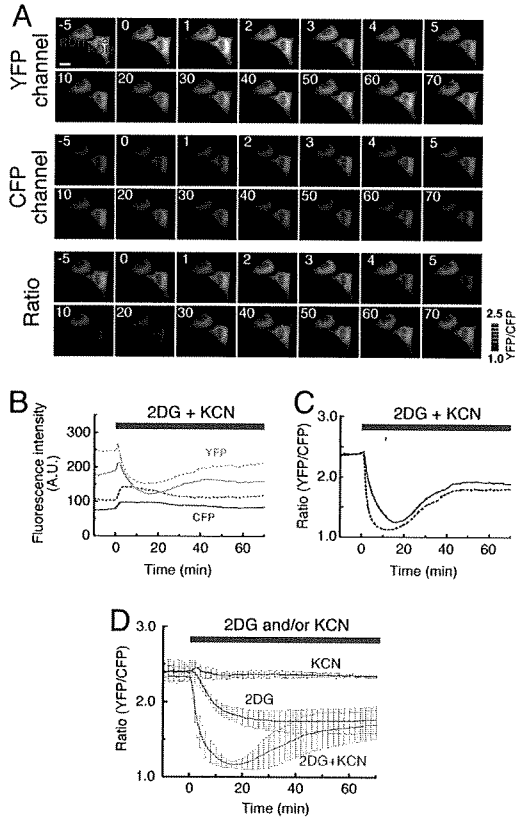

Fig. 5. Monitoring of cytoplasmic ATP levels of HeLa cells. (*A*) Sequential wide-field images of YFP (top), CFP (middle) and YFP/CFP emission ratio (bottom, pseudocolored) of a HeLa cell expressing AT1.03. Inhibitors of glycolysis (10 mM 2-deoxyglucose [2DG]) and OXPHOS (1 mM potassium cyanide [KCN]) were added at time = 0 (min). Elapsed time (in minutes) after addition of the inhibitors is shown to the top left of the cells. Images were obtained at 37 °C. (Scale bar, 20 μm). (*B*) Time course of fluorescence intensity of CFP (blue) and YFP (green) inside ROI1 (solid line) and ROI2 (dashed line) depicted in the top-left image of (*A*). (*C*) Time course of YFP/CFP emission ratio inside ROI1 (red solid line) and ROI2 (blue dashed line) depicted in the top-left image of (*A*). (*D*) Time course of averaged YFP/CFP emission ratio of HeLa cells expressing AT1.03. 2DG and/or potassium azide was added at time = 0 (min). Red, 2DG and KCN ($n = 5$); green, 2DG ($n = 6$); blue, KCN ($n = 4$). Error bars are standard deviations between measurements.

AT1.03$^{R122K/R126K}$ mutant by substituting the arginine residues with lysine residues. This mutant ATeam did not respond even to 10 mM ATP (Fig. S4*B*). Then, HeLa cells were observed with AT1.03$^{R122K/R126K}$. As expected, the cytoplasm, nucleus and mitochondria showed essentially the same level of the YFP/CFP emission ratio (Fig. 4*D*). Thus, it was confirmed that the ATP level in mitochondria is lower than that of cytoplasm or nucleus. However, the lower [ATP] level in mitochondria may seem paradoxical when we consider that mitochondria are the major ATP-producing organelles of cells. One possible explanation is that adenine nucleotide translocator pumps ATP from the mitochondria, thereby maintaining a high ADP/ATP ratio; this seems preferable for F_oF_1-ATP synthase to produce ATP from ADP and phosphate. One might point out that the low dependence on oxidative phosphorylation (OXPHOS) for ATP production of cancer cells like HeLa cells (23) (also see below) causes the low [ATP] in mitochondria. However, this possibility is unlikely, because we did not observe clear changes of both cytoplasmic and mitochondrial ATP level in HeLa cells grown in galactose medium (data not shown), whose major ATP-generating pathway is OXPHOS (see below). A lower [ATP] in mitochondria was also observed in noncancer NIH 3T3 cells (data not shown). For the generality and the mechanism of this phenomenon, further investigations remain to be done.

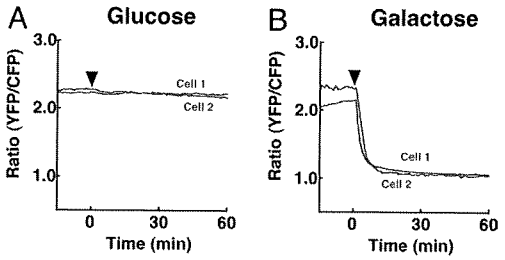

Fig. 6. Nutrient dependent alternation of ATP-generating pathway of HeLa cells. Sensitivity of intracellular ATP level to an OXPHOS inhibitor, oligomycin A, was examined for HeLa cells grown in glucose (*A*) or galactose (*B*) medium. Time courses of YFP/CFP emission ratio of cells expressing AT1.03, which were grown in DMEM without pyruvate containing 10 mM glucose (*A*) or 10 mM galactose (*B*), were monitored as in Fig. 5. Oligomycin A (10 μg/ml) was added to the medium at a time indicated by an arrow head.

Real-Time Monitoring of Intracellular ATP Depletion. We next monitored the dynamics of ATP levels in living HeLa cells after the addition of 2-deoxyglucose (2DG) and potassium cyanide (KCN), which are inhibitors of glycolysis and OXPHOS, respectively. Fig. 5*A* shows sequential images of the CFP and YFP channels. Addition of the inhibitors induced an increase in CFP intensity and a decrease in YFP intensity, which rapidly decreased the YFP/CFP emission ratio (i.e., decrease of [ATP]; Fig. 5 *A* and *C*). Interestingly, the cytoplasmic [ATP] partially recovered after the transient decay. This partial [ATP] recovery would be the result of a cellular response to a large decrease in intracellular [ATP]. Addition of 2DG alone also induced a decrease of [ATP], although the drop rate was much slower than when the two inhibitors were added. In addition, recovery of [ATP] was hardly observed. In contrast to 2DG, KCN itself had almost no effect on the intracellular ATP level. The result is consistent with the fact that ATP synthesis in actively proliferating cancer cells is mainly dependent on glycolysis, rather than OXPHOS in mitochondria, even in the aerobic environment (23). Our result showed that 2DG and KCN have a synergistic rather than additive effect on the intracellular ATP level, thereby suggesting that the intracellular ATP level is synergistically regulated by both glycolysis and OXPHOS. It has been shown that >80% of uptaken glucose is metabolized through glycolysis, when HeLa cells are grown in medium containing glucose (24). In contrast, when galactose is used in medium instead of glucose, most of galactose is metabolized through pentose phosphate pathway, and contribution of glutamine to generation of ATP through citrate cycle drastically increases (24). In addition, HeLa cells grown in galactose show elevated mitochondrial respiration rate and increased synthesis of mitochondrial proteins, as compared to those grown in glucose (25). Therefore, it is thought that ATP generation mainly depends on OXPHOS in the cells grown in galacotose medium. To confirm this, we compared changes of cytoplasmic [ATP] between cells grown in glucose and galactose in response to inhibition of F_oF_1-ATP synthase by oligomycin A. When oligomycin A was added to the cells grown in glucose medium, apparent change in cytoplasmic ATP level was not observed (Fig. 6*A*). This is consistent with the above result that OXPHOS inhibition by KCN did not affect cytoplasmic [ATP] (Fig. 5*D*). On the other hand, cytoplasmic [ATP] of HeLa cells grown in galactose was

rapidly depleted by the addition of oligomycin A. Cells did not show partial recovery of [ATP] in this experiment, unlike those grown in glucose medium and treated with 2DG and KCN (Fig. 5 *C* and *D*). These data clearly show that HeLa cells growing in galactose medium generate most of cellular ATP using OXPHOS, whereas those growing in glucose use glycolysis for ATP production. This flexible alternation of energy metabolism seems to be advantageous for the cells to propagate in glucose-limiting conditions.

Discussion

In this study, we report a method to measure intracellular ATP levels by using genetically-encoded FRET-based indicators for ATP, ATeams. These probes show high selectivity to ATP over other nucleotides. The affinity of ATeam to ATP is tunable by substituting the ε subunit with that from different species or changing the amino acid residues at the domain interface. In principle, it is possible to measure ATP levels at levels ranging from 2 μM to 8 mM by modulating the affinity of ATeam. Organelle-specific ATP level monitoring was also shown to be possible by targeting the probe to the nucleus and mitochondria. This method showed that the mitochondrial ATP level is unexpectedly lower than that in the cytoplasm. ATeam is potentially able to monitor any desired intracellular compartments by attaching a proper signal sequence or by fusion to a localized protein. ATeams can be used in broad fields of biological research. For example, ATeam might become a strong tool to study energy metabolism and mitochondrial function. In addition, estimation of intracellular ATP levels by ATeams might be a good way to evaluate cell viability or toxicity of chemicals, because dead cells lose intracellular ATP.

Materials and Methods

Chemicals. DNA polymerase and DNA ligation kits were purchased from TaKaRa; oligonucleotides were from Hokkaido System Science; restriction endonucleases were from Roche Diagnostics; ATP, ADP, GTP, and dATP were from Sigma; and other chemical reagents were from Wako Pure Chemicals, unless otherwise noted. ATP and other nucleotides were complexed with equimolar magnesium chloride ($MgCl_2$) before use in the experiments; therefore, the term ATP in this study means MgATP.

Gene Construction. *B. subtilis* ε subunit cDNA with humanized codons was synthesized by Hokkaido System Science. The synthesized cDNA also has V9T, V42K, F67N, and Leu78T mutations to disrupt a hydrophobic patch for interaction with the γ subunit of ATP synthase. The cDNA of mseCFPΔC11, the ε subunit, and cp173-mVenus was amplified by PCR (PCR) and then ligated. Ligated DNA was then ligated to XhoI-HindIII sites of the pRSET-B vector (Invitrogen) to obtain pRSET-AT1.03 for expression of AT1.03 in *Escherichia coli*, and to XhoI–HindIII sites of pcDNA3.1(−) (Invitrogen) to obtain pcDNA-AT1.03 for mammalian expression. pRSET-AT3.10, which is for expression of AT3.10 in *E. coli*, was constructed by replacing the mseCFPΔC11 part of pRSET-AT1.03 with mseCFPΔC10, and the *B. subtilis* ε part with *Bacillus* sp. PS3 ε, which has V9T, V42K, F67N and L78N mutations. PCR-based mutagenesis was used to construct pRSET-AT1.03^{YEMK} and pRSET-AT3.10^{MGK} from pRSET-AT1.03 and pRSET-AT3.10, respectively.

Purification of ATeam. *E. coli* strain JM109(DE3) carrying ATeam plasmid was cultured in LB medium at 37 °C for 3 h. Protein expression was then induced by adding 10 μM isopropyl-β-thiogalactopyranoside, followed by overnight incubation at 24 °C. Cells were collected by centrifugation, suspended in buffer A (100 mM sodium phosphate [pH 8.0], 200 mM sodium chloride, and 10 mM imidazole), and then disrupted by sonication. Cell-free extract, obtained by centrifugation at 10,000 × *g* for 60 min, was applied to a Ni-NTA column (Qiagen) preequilibrated with buffer A. After washing the column with buffer A, the protein was eluted by increasing the imidazole concentration to 200 mM. Fractions containing ATeam were concentrated, followed by application to a Superdex200 gel-filtration column (GE Healthcare) preequilibrated with 20 mM Tris·HCl (pH 8.0) and 150 mM sodium chloride. After adding glycerol to a final concentration of 20%, the purified ATeam protein was stored at −20 °C for further use.

Characterization of ATeam In Vitro. Protein concentration was determined using light absorption at 515 nm and the extinction coefficient of Venus protein ($\varepsilon = 92\ mM^{-1}cm^{-1}$)[16]. The fluorescence of purified ATeam proteins was investigated in buffer B (50 mM Mops-KOH [pH 7.3], 50 mM KCl, 0.5 mM $MgCl_2$, and 0.05% Triton X-100) using an FP-6500 spectrofluorometer (Jasco) at 37 °C. To obtain the fluorescence spectra, CFP was excited with 435 ± 20 nm light, and emission from 460 to 600 nm was scanned. To measure the time course of CFP emission change, CFP was excited using 435 ± 5 nm light and emission at 475 ± 10 nm was monitored by adding ATP at specific time points.

Cell Culture and Microscopy. HeLa cells were obtained from JCRB, and maintained in Dulbecco's modified Eagle's medium (DMEM, Sigma) supplemented with 10% FBS (Invitrogen). For glucose-free culture, cells were maintained in DMEM, which contains 10 mM galactose instead of glucose and is supplemented with 10% dialyzed FBS (Invitrogen). Cells were plated on a collagen-coated glass-bottom dish (FPI) and transfected with plasmid coding ATeam cDNA by using FuGENE6 transfection reagent (Roche Diagnostics). Between one and four days after transfection, cells cultured in phenol red-free DMEM were subjected to imaging. Wide-field observations of the cells were performed on a Nikon TE2000-PFS inverted microscope (Nikon Instruments) using a PlanApo VC60, 1.40 numerical aperture (NA), oil-immersion objective (Nikon). Filters used for dual-emission ratio imaging of ATeam were purchased from Semrock: an FF01–427/10 excitation filter, an FF458-Di01 dichroic mirror, and two emission filters (FF01–483/32 for CFP and FF01–542/27 for YFP). The two emission filters were alternated by using a filter changer (Ludl Electronic Products Ltd). Cells were illuminated using a 75-W xenon lamp through 12.5% and 25% neutral density filters. Fluorescence emission from ATeam was imaged by using a cooled charge-coupled device (CCD) camera (ORCA-AG; Hamamatsu Photonics); the exposure times were 500 ms for CFP and YFP images. Cells were maintained on a microscope at 37 °C with a continuous supply of a 95% air and 5% carbon dioxide mixture by using a stage-top incubator (Tokai Hit). Image analysis was performed using MetaMorph (Molecular Devices). The YFP/CFP emission ratio was calculated by dividing pixel-by-pixel a YFP image with a CFP image.

ACKNOWLEDGMENTS. We thank Tsuyoshi Nishi and Akihito Yamaguchi for providing us with the equipment for cell culture, Makoto Fujikawa for suggestion for culturing cell in galactose medium, Hiromasa Yagi and Hideo Akutsu for sharing the 3D coordinate crystal structure of ε subunit complexed with ATP before publishing, and Shigeko Kawai-Noma and Hideki Taguchi for plasmids for W1B mutants of CFP and YFP, which were used in the very early stage of this study. We are also indebted to all of the members of the Noji Laboratory for valuable discussions and advice. This work was supported by Grant-in-Aid for Scientific Research 18074005 and 18201025 (to H.N.) and Post-Silicon Materials and Devices Research Alliance (to T.N. and H.N.) from the Ministry of Education, Culture, Sports, Science and Technology of Japan and Precursory Research for Embryonic Science (to H.I.) from Japan Science and Technology Agency.

1. Ashcroft FM (2005) ATP-sensitive potassium channelopathies: Focus on insulin secretion. *J Clin Invest* 115:2047–2058.
2. Finger TE, et al. (2005) ATP signaling is crucial for communication from taste buds to gustatory nerves. *Science* 310:1495–1499.
3. Davalos D, et al. (2005) ATP mediates rapid microglial response to local brain injury *in vivo*. *Nat Neurosci* 8:752–758.
4. Masse K, Bhamra S, Eason R, Dale N, Jones EA (2007) Purine-mediated signalling triggers eye development. *Nature* 449:1058–1062.
5. Kennedy HJ, et al. (1999) Glucose generates sub-plasma membrane ATP microdomains in single islet β-cells. Potential role for strategically located mitochondria. *J Biol Chem* 274:13281–13291.
6. Gribble FM, et al. (2000) A novel method for measurement of submembrane ATP concentration. *J Biol Chem* 275:30046–30049.
7. Tsuboi T, Lippiat JD, Ashcroft FM, Rutter GA (2004) ATP-dependent interaction of the cytosolic domains of the inwardly rectifying K^+ channel Kir6.2 revealed by fluorescence resonance energy transfer. *Proc Natl Acad Sci USA* 101:76–81.
8. Berg J, Hung YP, Yellen G (2009) A genetically encoded fluorescent reporter of ATP:ADP ratio. *Nat Methods* 6:161–166.
9. Kato-Yamada Y, et al. (1999) ε subunit, an endogenous inhibitor of bacterial F_1-ATPase, also inhibits F_oF_1-ATPase. *J Biol Chem* 274:33991–33994.
10. Rondelez Y, et al. (2005) Highly coupled ATP synthesis by F_1-ATPase single molecules. *Nature* 433:773–777.
11. Suzuki T, et al. (2003) F_oF_1-ATPase/synthase is geared to the synthesis mode by conformational rearrangement of ε subunit in response to proton motive force and ADP/ATP balance. *J Biol Chem* 278:46840–46846.
12. Kato-Yamada Y, Yoshida M (2003) Isolated ε subunit of thermophilic F_1-ATPase binds ATP. *J Biol Chem* 278:36013–36016.
13. Iino R, et al. (2005) Real-time monitoring of conformational dynamics of the ε subunit in F_1-ATPase. *J Biol Chem* 280:40130–40134.
14. Yagi H, et al. (2007) Structures of the thermophilic F_1-ATPase ε subunit suggesting ATP-regulated arm motion of its C-terminal domain in F_1. *Proc Natl Acad Sci USA* 104:11233–11238.

15. Matsuda T, Miyawaki A, Nagai T (2008) Direct measurement of protein dynamics inside cells using a rationally designed photoconvertible protein. *Nat Methods* 5:339–345.
16. Nagai T, et al. (2002) A variant of yellow fluorescent protein with fast and efficient maturation for cell-biological applications. *Nat Biotechnol* 20:87–90.
17. Zacharias DA, Violin JD, Newton AC, Tsien RY (2002) Partitioning of lipid-modified monomeric GFPs into membrane microdomains of live cells. *Science* 296:913–916.
18. Nagai T, Yamada S, Tominaga T, Ichikawa M, Miyawaki A (2004) Expanded dynamic range of fluorescent indicators for Ca^{2+} by circularly permuted yellow fluorescent proteins. *Proc Natl Acad Sci USA* 101:10554–10559.
19. Kato-Yamada Y (2005) Isolated ε subunit of *Bacillus subtilis* F_1-ATPase binds ATP. *FEBS Lett* 579:6875–6878.
20. Kato S, Yoshida M, Kato-Yamada Y (2007) Role of the ε subunit of thermophilic F_1-ATPase as a sensor for ATP. *J Biol Chem* 282:37618–37623.
21. Llopis J, McCaffery JM, Miyawaki A, Farquhar MG, Tsien RY (1998) Measurement of cytosolic, mitochondrial, and Golgi pH in single living cells with green fluorescent proteins. *Proc Natl Acad Sci USA* 95:6803–6808.
22. Filippin L, et al. (2005) Improved strategies for the delivery of GFP-based Ca^{2+} sensors into the mitochondrial matrix. *Cell Calcium* 37:129–136.
23. Warburg O (1956) On respiratory impairment in cancer cells. *Science* 124:269–270.
24. Reitzer LJ, Wice BM, Kennell D (1979) Evidence that glutamine, not sugar, is the major energy source for cultured HeLa cells. *J Biol Chem* 254:2669–2676.
25. Rossignol R, et al. (2004) Energy substrate modulates mitochondrial structure and oxidative capacity in cancer cells. *Cancer Res* 64:985–993.

Plant Physiology Preview. Published on May 27, 2009, as DOI:10.1104/pp.109.139329

Running head: Ca^{2+} dynamics in the pollen tube

Corresponding author: Megumi Iwano, 8916-5 Takayama, Ikoma, Nara 630-0101, JAPAN, E-mail, m-iwano@bs.naist.jp, Tel: (+81) 743 72 5453, Fax: (+81) 743 72 5459.

Subject area: Cell biology

Title: Fine tuning of the cytoplasmic Ca^{2+} concentration is essential for pollen tube growth

Authors: Megumi Iwano[1*], Tetsuyuki Entani[1], Hiroshi Shiba[1], Mituru Kakita[1], Takeharu Nagai[3], Hideaki Mizuno[2], Atsushi Miyawaki[2], Tsubasa Shouji[1], Kenichi Kubo[1], Akira Isogai[1] and Seiji Takayama[1]

[1]Graduate School of Biological Sciences, Nara Institute of Science and Technology, Ikoma, Nara 630-0101, Japan.

[2] Brain Science Institute, The Institute of Physical and Chemical Research (RIKEN), Wako, Saitama 351-0198, Japan.

[3] Research Institute for Electronic Science, Hokkaido University, Sapporo, Hokkaido 060-0812, Japan

Abstract

Pollen tube growth is crucial for the delivery of sperm cells to the ovule during flowering plant reproduction. Previous *in vitro* imaging of *Lilium longiflorum* and *Nicotiana tabacum* has shown that growing pollen tubes exhibit a tip-focused Ca^{2+} concentration ($[Ca^{2+}]$) gradient and regular oscillations of the cytosolic $[Ca^{2+}]$ ($[Ca^{2+}]_{cyt}$) in the tip region. Whether this $[Ca^{2+}]$ gradient and/or $[Ca^{2+}]_{cyt}$ oscillations are present as the tube grows through the stigma (*in vivo* condition), however, is still not clear. We monitored $[Ca^{2+}]_{cyt}$ dynamics in pollen tubes under various conditions using *Arabidopsis* and *N. tabacum* expressing yellow cameleon 3.6, a fluorescent calcium indicator with a large dynamic range. The tip-focused $[Ca^{2+}]_{cyt}$ gradient was always observed in growing pollen tubes. Regular oscillations of the $[Ca^{2+}]_{cyt}$, however, were rarely identified in *Arabidopsis* or *N. tabacum* pollen tubes grown under the *in vivo* condition, or in those placed in germination medium just after they had grown through a style (semi-*in vivo* condition). On the other hand, regular oscillations were observed *in vitro* in both growing and nongrowing pollen tubes, although the oscillation amplitude was 5-fold greater in the nongrowing pollen tubes compared with growing pollen tubes. These results suggested that a submicromolar $[Ca^{2+}]_{cyt}$ in the tip region is essential for pollen tube growth, whereas a regular $[Ca^{2+}]$ oscillation is not. Next, we monitored $[Ca^{2+}]$ dynamics in the endoplasmic reticulum ($[Ca^{2+}]_{ER}$) in relation to *Arabidopsis* pollen tube growth using yellow cameleon 4.6, which has a lower affinity for Ca^{2+} compared with yellow cameleon 3.6. The $[Ca^{2+}]_{ER}$ in pollen tubes grown under the semi-*in vivo* condition was between 100 and 500 μM. In addition, cyclopiazonic acid (CPA), an inhibitor of ER-type Ca^{2+}-ATPases, inhibited growth and decreased the $[Ca^{2+}]_{ER}$. Our observations suggest that the ER serves as one of Ca^{2+} stores in the pollen tube and CPA-sensitive Ca^{2+}-ATPases in the ER are required for pollen tube growth.

In many flowering plants, a pollen grain that lands on the top surface of a stigma will hydrate and germinate a pollen tube. Following germination, the pollen tube enters the style and grows through the wall of transmitting tract cells on the way to the ovary, where the tube emerges to release the sperm for double fertilization. Therefore, pollen tube growth is essential for reproduction in flowering plants.

Since Brewbaker and Kwack revealed that Ca^{2+} is essential for *in vitro* pollen tube cultures (1963), the relationship between the Ca^{2+} concentration ($[Ca^{2+}]$) and pollen tube growth has been further examined under *in vitro* germination culture conditions. Ratiometric ion imaging using fluorescent dye has revealed that the apical domain of a pollen tube grown *in vitro* contains a tip-focused $[Ca^{2+}]$ gradient (Pierson et al., 1994; Pierson et al., 1996; Cheung & Wu, 2008), and that the cytoplasmic $[Ca^{2+}]$ ($[Ca^{2+}]_{cyt}$) in the tip region and the growth rate oscillate with the same periodicity (Holdaway-Clarke et al., 1997; Messerli & Robinson, 1997; Pierson et al., 1996). Therefore, oscillation of the $[Ca^{2+}]_{cyt}$ has been thought to correlate with pollen tube growth. It is not clear, however, whether regular $[Ca^{2+}]_{cyt}$ oscillations in the tip region occur in pollen tubes growing through stigmas and styles.

The $[Ca^{2+}]_{cyt}$ is controlled temporally and spatially by transporters in the membranes of intracellular compartments and in the plasma membrane (Sze et al., 2000). Studies using a Ca^{2+}-sensitive vibrating electrode revealed Ca^{2+} influx in the tip region of the pollen tube (Pierson et al., 1994; Holdaway-Clarke et al., 1997; Franklin-Tong et al., 2002). Stretch-activated Ca^{2+} channels have been found in the plasma membrane using patch-clamp electrophysiology (Kuhtreiber & Jaffe, 1990; Dutta & Robinson, 2004). Recently, CNGC18 was identified as a Ca^{2+}-permeable channel in the plasma membrane that is essential for pollen tube growth (Frietsch et al., 2007). The intracellular compartments that store Ca^{2+} in the pollen tube and the relevant Ca^{2+} transporters, however, have yet to be identified.

Yellow cameleons are genetically encoded Ca^{2+} indicators that were developed to monitor the [Ca^{2+}] in living cells (Miyawaki et al., 1997). These indicators are chimeric proteins consisting of enhanced cyan fluorescent protein (ECFP), calmodulin (CaM), a glycylglycine linker, the CaM-binding domain of myosin light chain kinase (M13), and enhanced yellow fluorescent protein (EYFP). When the CaM domain binds Ca^{2+}, the domain associates with the M13 peptide and induces fluorescence resonance energy transfer (FRET) between ECFP and EYFP. Several types of cameleons have been developed by tuning the CaM domain binding affinity for Ca^{2+}. Yellow cameleon 2.1 (YC2.1) is a high-affinity indicator that has been used to monitor the $[Ca^{2+}]_{cyt}$ in *Arabidopsis* guard cells (Allen et al., 1999; 2000; 2001), *Lilium longiflorum* and *Nicotiana tabacum* pollen tubes (Watahiki et al., 2004), and the root hair of *Medicago* (Miwa et al., 2006). YC3.1 is a low-affinity indicator that has been used to monitor the $[Ca^{2+}]_{cyt}$ during pollen germination and in papilla cells of *Arabidopsis* (Iwano et al., 2004).

Recently, YC3.60 was developed as a new YC variant (Nagai et al., 2004), in which the acceptor fluorophore is a circularly permuted version of Venus rather than EYFP (Nagai et al., 2002). YC3.60 has a monophasic Ca^{2+} dependency with a dissociation constant (*K'*d) of 0.25 μM. Compared with YC3.1, YC3.60 is equally bright with a 5- to 6-fold larger dynamic range. Thus, YC3.60 results in a markedly enhanced signal-to-noise ratio, thereby enabling Ca^{2+} imaging experiments that were not possible with conventional YCs. On the other hand, YC4.60 was developed by mutating the Ca^{2+}-binding loop of CaM in YC3.60. Because YC4.60 has a significantly lower Ca^{2+} affinity with a biphasic Ca^{2+} dependency (*K'*d: 58 nM and 14.4 μM), it allows changes in [Ca^{2+}] dynamics to be detected against a high background [Ca^{2+}] (Nagai et al., 2004).

To examine whether the $[Ca^{2+}]_{cyt}$ oscillates in pollen tubes growing through a stigma after pollination (*in vivo* condition), in those placed in germination medium